FLORIDA STATE UNIVERSITY

COLLEGE OF ARTS AND SCIENCES

γ-RAY SPECTROSCOPIC STUDY OF CALCIUM-48,49 AND SCANDIUM-50

FOCUSING ON LOW LYING OCTUPOLE VIBRATION EXCITATIONS

By

DAVID M. MCPHERSON

A Dissertation submitted to the
Department of Physics
in partial fulfillment of the
requirements for the degree of
Doctor of Philosophy

2015

ProQuest Number: 3724324
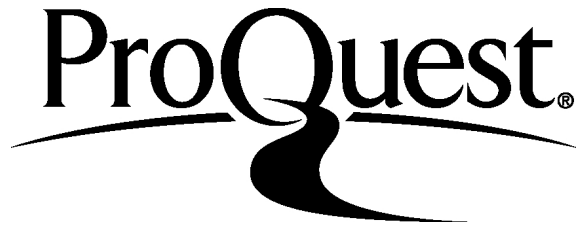
ProQuest.

ProQuest 3724324

Published by ProQuest LLC (2015). Copyright of the Dissertation is held by the Author.

ProQuest LLC.
789 East Eisenhower Parkway
P.O. Box 1346
Ann Arbor, MI 48106 - 1346

David M. McPherson defended this dissertation on July 8, 2015.
The members of the supervisory committee were:

Paul Cottle

Professor Directing Dissertation

Alec Kercheval

University Representative

Jianming Cao

Committee Member

Jorge Piekarewicz

Committee Member

Mark Riley

Committee Member

The Graduate School has verified and approved the above-named committee members, and certifies that the dissertation has been approved in accordance with university requirements.

To the love of my life, Toby, who has been so supportive of my work and progress

ACKNOWLEDGMENTS

Over the course of my PhD career, I have encountered so many people who have guided me and helped me get to this point, and as much as I would like to take the time to thank each and every one it is possible I would take up just as many pages as there are in this dissertation in the first place.

To start off, I want to thank my major professor, Dr. Paul Cottle, for his patience and guidance of my doctorate work. As much of a headache as I may have been over the years, he has diligently worked with me to overcome my weaknesses and difficulties as well as focus my skills to the completion of this dissertation. I also want to thank Dr. Lew Riley for sharing his knowledge and expertise in the analysis method used in this dissertation. We've had quite a few interesting discussions about how to analyze the data from e11037, and his ability to communicate via email has been very effective in describing the methods and procedures used in this dissertation. I thank both Cottle and Riley for the opportunity to perform my doctoral research at the National Superconducting Cyclotron Laboratory at Michigan State University, as it was an amazing experience in and out of the laboratory.

I would like to thank my committee members, Professors Jianming Cao, Alec Kercheval, Jorge Piekarewicz, and Mark Riley, for their support, guidance, and assistance over the past few years not only for the course of this dissertation, but for their advice in professionalism and perseverance as well. In addition, I would also like to thank Professors Kirby Kemper, Alexander Volya, Ingo Wiedenhover, Vandana Tripathi, and Simon Capstick for their assistance in learning the basic principles of nuclear experimental and theoretical physics. At Michigan State Unversity, I would like to thank Drs. Remco Zegers, Dirk Weisshar, Alexandra Gade, and Shumpei Noji for their assistance and guidance with the installation of the liquid hydrogen target as well as performance of the three experiments with the target, including my own.

I would like to give a special thanks to Dr. David Caussyn for his assistance and maintenance of the computer terminals used during the analysis of the data from e11037, as well as helping me gain a better understanding of computer programming in general. To that effect, I would also like to thank Pei-Luan Tai for exposing me to shell scripting techniques that were instrumental in automating my analysis of the data, as well as Jonathan Baron for serving as a sounding board

iv

for my physical and computer programming arguments. Without both of them, my analysis would have taken twice as long to complete.

Over the course of my career, it has sometimes been difficult to take the time to relax and let my mind breathe. I have had several friends help me do this over the years, including, but not limited to, Rodney Ferguson, Matthew Fulmer, Brett Thomas, Seth Anderson, and Timothy Farmer. They have all helped me stop and unwind when my brain tried to pummel through. I would also like to thank Jory Collette for our discussions over the past few years, serving as my mental and emotional sounding board when things got too tough to handle on my own, as well as Ashley Hammond and Ludmilla De Faria.

My progress as a physics student would have been immeasurably more difficult without my family supporting me. My mother, Dianne McPherson, has always believed in me, as has my sister, Madonna Dunn. My uncle, James Tate, should also be mentioned and thanked for his financial support. I also want to thank my love and partner, Toby McClellan, for his guidance and support over the past year and a half. Without him, it would have been difficult to find meaning in my career.

TABLE OF CONTENTS

LIST OF TABLES

LIST OF FIGURES

ABSTRACT

An inverse kinematic proton scattering experiment was performed at the National Superconducting Cyclotron Laboratory (NSCL) using the GRETINA-S800 detector system in conjunction with the Ursinus College liquid hydrogen target. γ-ray yields from the experiment were determined using GEANT4 simulations, generating state population cross sections. These cross sections were used to extract the δ_3 deformation length for the low-lying octupole vibration excitations in ^{48,49}Ca using the coupled channels analysis code FRESCO. Particle-core coupling in ^{49}Ca was studied in comparison to ^{48}Ca through determination of the neutron and proton deformation lengths.

The total inverse kinematic proton scattering deformation lengths were evaluated for the low-lying octupole vibration excitations in ^{48,49}Ca to be $\delta_3\left(^{48}Ca, 3_1^-\right) = 1.0(2)$fm, $\delta_3\left(^{49}Ca, \frac{9}{2}_1^+\right) = 1.2(1)$fm, $\delta_3\left(^{49}Ca, \frac{7}{2}_1^+\right) = 1.5(2)$fm, $\delta_3\left(^{49}Ca, \frac{5}{2}_1^+\right) = 1.1(1)$fm. Proton and neutron deformation lengths for two of these octupole states were also determined to be $\delta_p\left(^{48}Ca, 3_1^-\right) = 0.9(1)$fm, $\delta_p\left(^{49}Ca, \frac{9}{2}_1^+\right) = 1.0(1)$fm, $\delta_n\left(^{48}Ca, 3_1^-\right) = 1.1(3)$fm, and $\delta_n\left(^{49}Ca, \frac{9}{2}_1^+\right) = 1.3(3)$fm. Additionally, the ratios of the neutron to proton transition matrix elements were also determined for these two states to be $M_n/M_p\left(^{48}Ca, 3_1^-\right) = 1.7(6)$ and $M_n/M_p\left(^{49}Ca, \frac{9}{2}_1^+\right) = 2.0(5)$. Statistically, the results for ^{49}Ca are identical to ^{48}Ca, which indicates that the valence neutron coupled to the ^{48}Ca core produces statistically negligible differences in the lowest-lying octupole vibration of ^{49}Ca.

CHAPTER 1

FOUNDATION

Nuclear physics is a rapidly expanding research field focused on improving the understanding of the fundamental interactions inside of the nucleus as well as learning the origins of the known elements in the universe. The extensive range of known, bound nuclei exhibit a variety of nuclear phenomena that become focal points in nuclear research. One phenomenon in particular is the fact that nuclei with specific numbers of protons and/or neutrons require more energy to separate those protons and/or neutrons. These numbers, $Z, N = 2, 8, 20, 28, 50, 82$, and 126, were termed "magic" numbers. The idea of nuclear shell structure, similar to the atomic shell structure of the electron cloud surrounding the nucleus, was able to explain these numbers. Protons and neutrons fill nuclear orbital shells according to selection rules of angular momentum, spin, and the Pauli exclusion principle. These shell structure models described the microscopic picture of the nucleus and the behavior of individual nucleons interacting with the average nuclear field.

However, these numbers were primarily observed for isotopes near what became known as the valley of stability in the chart of nuclides. As mentioned in *The Frontiers of Nuclear Science, A Long Range Plan*, as nuclear research expanded the range of known, bound nuclei in the chart of nuclides some isotopes were found to ignore the magic numbers while other nuclei were found to exhibit the behavior of magic numbers with different nucleon numbers, such as $N = 14, 16, 32$ and $Z = 14$ [5]. This suggested the collapse of shell closures at the standard magic numbers and new sub-shell closures at new magic numbers, especially in neutron heavy nuclei toward the neutron drip-line, the furthest extent of bound neutron rich isotopes on the chart of nuclides.

With this in mind, an experiment was proposed to study the $N = 32$ sub-shell closure. Using a liquid hydrogen (LH_2) target, the experiment would focus on obtaining γ-ray spectroscopic information on ^{50,52}Ca as outlined in the proposal Dr. Lew Riley submitted to the National Superconducting Cyclotron Laboratory (NSCL) Program Advisory Committee [6]. The goal was to analyze the low-lying 2^+ state in ^{50,52}Ca to gain information on the suspected sub-shell closure in ^{52}Ca. The data in the experiment not only included inverse kinematic proton scattering data

from the reaction of ^{50,52}Ca with the proton target, it also contained ^{48,49}Ca and ^{50}Sc reaction data. As part of the effort to establish nuclear shell structure information leading up to ^{50,52}Ca and the $N = 32$ sub-shell closure, the present analysis focused on extracting shell structure data on the ^{49}Ca nucleus, with complimentary analyses on ^{48}Ca and ^{50}Sc.

Prior to this analysis, there was a substantial amount of data available on the ^{48}Ca nucleus as it is a stable isotope. According to Balysh, *et al*, the ^{48}Ca ground state has only one possible decay channel, the double $\beta\beta_{2\nu}$ decay, and they measured the half-life of the ^{48}Ca ground state to be on the order of 4.3×10^{19} years [7]. The level scheme for this nucleus, and the associated γ-ray energy decays, had been well established by a plethora of experiments, ranging from $^{48}Ca(e, e')$ and $^{48}Ca(d, d')$ reactions to polarized $^{48}Ca(p, p')$ and $^{48}Ca(^{48}Ca,^{48}Ca'\gamma)$ measurements. Previous analyses had been performed on the low-lying quadrupole and octupole vibrations for this nucleus and were used as a point of comparison in the present analysis for ^{48}Ca. Less was known about the ^{49}Ca nucleus, given its half-life of 8.7 minutes [8]. Low-lying energy states, and their associated γ-ray decays, were established using $^{48}Ca(d, p)$, $^{48}Ca(d, p\gamma)$, and various other transfer reactions. Even less was known about the ^{50}Sc nucleus with its ground state half-life of 102.5 seconds and isomeric state at an energy of about 257keV with a half-life of 0.35 seconds [9][10]. Only a few states and γ-ray decays had been established for this nucleus from $^{48}Ca(^3He, p)$ and $^{48}Ca(\alpha, d)$ reactions.

In addition to nuclear shell structure models, another model scheme was developed to describe the behaviors of the nucleus. The liquid drop models discuss the collective and coherent behavior and motion of nucleons as a whole. These models help account for phenomena such as the average density of protons and neutrons being roughly even across the entire nucleus, functioning as a nearly incompressible fluid that can be deformed, rotated, and undergo vibrations [11]. All nuclei exhibit behaviors predicted by both collective and shell models to some degree. In fact, collective behaviors can be modified by shell structure effects, and vice versa. This can be studied in nuclei near magic numbered nuclei. These magic nuclei have closed shells, and can exhibit collective behaviors in the form of vibrations. The degree to which these collective vibrations in these closed-shell cores are modified by shell structure effects can be seen by coupling valence nucleons to these cores. An example of this system would be the particle-core coupling of the valence neutron in ^{49}Ca to the ^{48}Ca core.

The primary question posed by this dissertation is by how much are the collective vibrations in ^{48}Ca modified by the coupling of a valence neutron. The inverse kinematic proton scattering experiment performed by Riley was very useful as the interaction of the proton probe with the components of the nucleus is fairly well understood. In low energy reactions, $E_p \sim 10\text{MeV}$, the proton probe interacts with the neutron component three times more strongly than the proton component, while in high energy reactions, $E_p > 1\text{GeV}$, the proton and neutron components are nearly indistinguishable to the proton probe [12].

Another interesting phenomenon in nuclear physics is the fact that the proton and neutron components of the nucleus can be described to act almost independent of each other, each one filling separate shells within the shell model as well as being described as two separate nuclear fluids superimposed on one another. The shape of each fluid can be described by the relation [13]

$$R\left(\theta, \phi\right) = R_0 \left(1 + \alpha_{00} + \sum_{\lambda=1}^{\infty} \sum_{\mu=-\lambda}^{\lambda} \alpha_{\lambda\mu}^* Y_{\lambda\mu}\left(\theta, \phi\right)\right) \quad (1.1)$$

where R_0 is the average nuclear size, $Y_{\lambda\mu}$ are the spherical harmonics functions, and $\alpha_{\lambda\mu}$ are the physical deformation parameters. For permanent deformations, the parameters $\alpha_{\lambda\mu}$ are constants, but for vibrations they are functions of time. The ground states of nuclei close to and at closed shells exhibit mostly spherical behavior, yielding $\alpha_{\lambda\mu} = 0$. When the nucleus is excited by an external probe, such as electrons, protons, or neutrons, it can be deformed initially and undergo vibrational motion until it deexcites back to the ground state by γ-ray decay.

For the present analysis, the low-lying octupole ($\lambda = 3$) vibrations in ^{48,49}Ca were chosen as the point of study for this dissertation. A comparison of the first substate ($\mu = 0$) of the pure quadrupole and octupole shapes is shown in Figure 1.1. The parameter, $\alpha_{3\mu}$, is the key to understanding the octupole vibrational motion of the proton and neutron components of ^{48,49}Ca. The parameter β_3, as a root-mean-square of the parameter $\alpha_{3\mu}$, modifies the octupole spherical harmonics in Equation 1.1, yielding the average shape of the nucleus undergoing a pure octupole vibration. This parameter, β_3, when multiplied by the average nuclear size, R_0, becomes the average octupole nuclear deformation length, δ_3. This deformation length is a measure of how much the ^{48,49}Ca nuclei are deformed by a proton scattering probe as they undergo octupole vibrations.

In homogeneous collective models, the proton and neutron components of the nucleus vibrate with the same amplitude, and thus would be deformed by the same amount, δ_3. However, Bernstein,
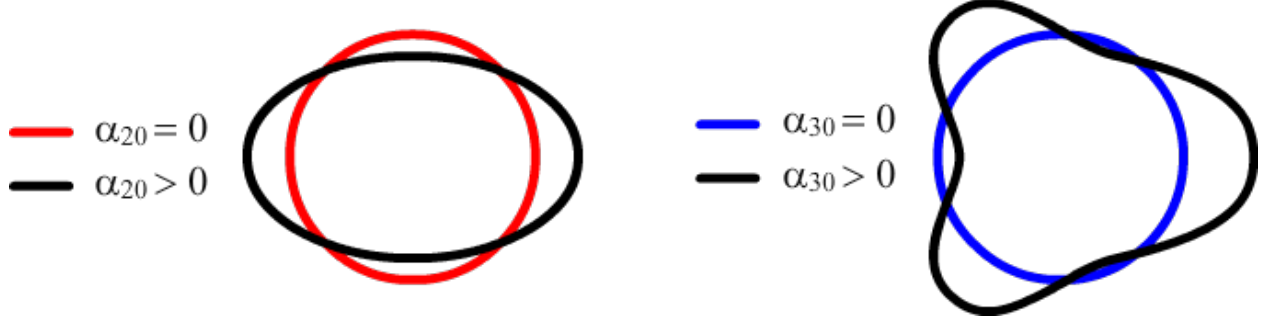
Figure 1.1: Comparison of $\mu = 0$ substates of pure quadrupole, $\lambda = 2$, and octupole, $\lambda = 3$, deformations.

Brown, and Madsen, showed that this is not the case for all nuclei [12]. The homogeneous collective model they describe predicts that the ratio of the neutron to proton transition matrix elements, M_n/M_p, equals the ratio of neutrons to protons, N/Z. However, when they compared the M_n/M_p ratios generated from experimental data for a large range of Ca, Ni, Sn, and other isotopes to the homogeneous collective model prediction, the two ratios did not match. Bernstein, Brown, and Madsen showed that the ratio M_n/M_p is proportional to the ratio N/Z by another ratio [12]

$$\frac{M_n}{M_p} = \frac{N\delta_n}{Z\delta_p} \tag{1.2}$$

where $\delta_{n(p)}$ is the neutron (proton) deformation length. The ratio of the two nucleon deformation lengths is not always one. For example, for the low-lying octupole vibrations in ^{208}Pb and ^{209}Bi the proton and neutron deformation lengths are not equal, as shown in Table 1.1.

The average, total nuclear deformation length, δ_3, contains both the proton and the neutron deformation lengths as both fluids are deformed by the external probe depending on the interaction strength of the probe with the nucleon types. Electromagnetic probes, such as electron probes for example, will only interact with the proton component of the nucleus as the neutrons are charge neutral. This fact is used later on in generating proton deformation lengths from previous measurements in heavy-ion transfer reactions. The total nuclear deformation length generated by a probe F is related to the proton and neutron deformation lengths by [11]

$$\delta^F = \frac{b_n^F N\delta_n + b_p^F Z\delta_p}{b_n^F N + b_p^F Z} \tag{1.3}$$

Table 1.1: M_n/M_p ratios for octupole states ^{208}Pb and ^{209}Bi, along with δ_n and δ_p. Uncertainties in all values shown in parentheses in last digit of values.

	J^π [$\hbar$]	E_{level} [MeV]	M_n/M_p	$\frac{M_n/M_p}{N/Z}$	δ_p [fm]	δ_n [fm]
^{208}Pb^{a,b}	3^-	2.614	1.24(6)	0.8(1)	1.05(4)	0.85(3)
^{209}Bi^{c,d}	$\frac{3}{2}^+$	2.494	0.22(1)	0.14(1)	0.605(5)	0.090(1)
	$\frac{9}{2}^+$	2.566	0.52(1)	0.34(1)	0.716(5)	0.246(2)
	$\frac{7}{2}^+$	2.585	0.46(1)	0.30(1)	0.672(5)	0.203(2)
	$\frac{11}{2}^+$	2.598	0.97(1)	0.63(1)	0.736(6)	0.471(4)
	$\frac{13}{2}^+$	2.600	1.03(1)	0.67(1)	0.706(5)	0.478(1)
	$\frac{5}{2}^+$	2.618	0.39(1)	0.26(1)	0.629(6)	0.161(1)
	$\frac{15}{2}^+$	2.744	0.95(1)	0.62(1)	0.577(5)	0.361(3)

^{a}$B(E3)$ value taken from Reference [14].

^{b}β_3 value taken from Reference [15].

^{c}$B(E3)$ values taken from Reference [16].

^{d}β_3 values values taken from Reference [17].

where $\delta^F = \delta_3$, and $b_{n(p)}^F$ is the neutron (proton) interaction strength of the probe F with the mean field of the target nucleus. By comparing δ_3 to the proton deformation length generated from lifetime measurements derived from heavy-ion transfer reactions, the neutron deformation lengths were derived.

This dissertation describes the process of performing and analyzing data taken from the inverse kinematic proton scattering experiment involving a rare isotope beam containing ^{48,49}Ca and ^{50}Sc conducted at the NSCL. γ-ray yields recorded by the Gamma Ray Energy Tracking In-beam Nuclear Array (GRETINA) in coincidence with the S800 detector system were sorted focusing on particle identification of elastic and inelastic reactions of the ^{48,49}Ca and ^{50}Sc particles with protons inside the Ursinus College LH_2 target. Measurements of the low-lying octupole vibration population cross sections were used in conjunction with coupled channels calculations using the analysis code FRESCO to extract the δ_3 values for these vibrational states. By comparison with lifetime measurements conducted by Montanari, *et al*, and subsequent generation of the proton deformation lengths, the neutron deformation lengths of the octupole vibrations of ^{48,49}Ca were determined. As part of the verification of the analysis method, ^{48}Ca was analyzed primarily to reproduce the previously known M_n/M_p ratio as well as comparable γ-ray yields generated by Lew Riley. In addition to

the calcium isotopes, a γ-ray spectroscopic study was performed on ^{50}Sc included in the proton scattering experiment.

The results of the present analysis, specifically the determination of the neutron deformation lengths, were used to study the particle-core coupling between the valence neutron in ^{49}Ca to the ^{48}Ca core. Differences between the neutron deformation lengths between these two nuclei, as well as differences between the proton deformation lengths, indicated the strength of this particle-core coupling. As will be shown later, the results showed no statistical difference in the neutron deformation lengths between ^{48}Ca and ^{49}Ca, as well as the proton deformation lengths between these nuclei. This indicated that the coupling of the valence neutron produces statistically negligible differences in the low-lying octupole vibrations in ^{49}Ca as compared to the low-lying octupole vibration excitations in ^{48}Ca.

Chapter 2 describes in detail the experimental setup of the inverse kinematic proton scattering experiment at the NSCL, including details on the LH_2 target and GRETINA-S800 detector system. Chapter 3 is devoted to the analysis of the raw data taken from the experiment, resulting in γ-ray yields and measured cross sections from ^{48,49}Ca and in trace amounts ^{50}Sc. Chapter 4 focuses on discussing the coupled channels calculations, their limitations, and applications to the understanding the particle-core couplingg in ^{49}Ca. In addition, Chapter 4 presents discussions on comparisons of the derived values to previously known data on ^{48,49}Ca. Chapter 5 concludes this dissertation with a basic summary and discussion of further research.

CHAPTER 2

EXPERIMENT

The experiment performed at the NSCL at MSU will be referred to throughout this dissertation using the label e11037. The experiment began with production of the rare isotope beam including the isotopes ^{48,49}Ca and ^{50}Sc. Once generated in sufficient intensities, this beam was guided to the S3 vault that contained the LH_2 target provided by Ursinus College. During the experiment, data was collected and recorded by the GRETINA-S800 detector system in place at the time.

2.1 Isotope Production

The process of generating the rare isotope beam started with ionization of the primary beam consisting of natural ^{76}Ge. The stable element was heated to temperatures in excess of $2000°C$, stripping it of electrons, then injected into the cyclotron beamline. While operating on the same principle as other cyclotrons, the K500 and K1200 cyclotrons are uniquely designed using three "dees", as shown in Figure 2.1. These cyclotrons produce a static magnetic field to keep the ionized ^{76}Ge in a confined spiral path. The "dees" of the cyclotron produce an oscillating electric field that propel the positive ions between them, accelerating the ions with each pass between the "dees". The reference frequency of the cyclotrons for the duration of e11037 was set at 22.5MHz. The K500 cyclotron initially accelerated the ^{76}Ge^{12+} ions to an energy of 11.6 MeV/u, and after the beam was stripped again to ^{76}Ge^{30+} the K1200 pumped the beam up to the final primary beam energy of 130MeV/u [18].

After exiting the coupled cyclotrons, the primary beam was fragmented by a 376 mg/cm^2 ^{9}Be crystal target and filtered by the A1900 fragment separator [19]. The reaction of the light ^{9}Be nucleus with the ^{76}Ge primary beam produced a plethora of exotic nuclei, including the nuclei of interest to this dissertation. The A1900 fragment separator was designed to separate these secondary beam particles to focus on production of specific nuclei. The dipole magnets of the A1900 bend the trajectories of the particles in the beamline, as shown in Figure 2.3, and were tuned to guide nuclei of interest through the beamline while removing nuclei of little consequence. In addition

to the dipole magnets, an aluminum wedge was used to further remove nuclei in the secondary beam [20]. The principal investigator, Dr. Lew Riley, was interested in reactions involving ^{50,52}Ca, and so the A1900 settings were optimized to maximize the production of ^{50}Ca. The resulting secondary beam produced for e11037 generated 73 ^{50}Ca particles per second (pps), 0.78 ^{52}Ca pps, 95 ^{49}Ca pps, 11.5 ^{48}Ca pps, and 3.9 ^{50}Sc pps [21].

Despite the optimization for the production of ^{50}Ca, the primary constituent of the secondary beam was identified as ^{47}K. This identification, along with the reference frequency, was used in the particle identification process explained in a later section. This focused secondary beam was guided down the I-beamline to the S3 vault containing the LH_2 target and the GRETINA-S800 detector system.

2.2   S800

Within the pit of the S3 vault rests the S800 Spectrograph, a high resolution, large acceptance mass spectrometer. This immense detector system starts at the entrance to the vault itself, referred to as the object of the S800, shown in Figure 2.4. Particles passing through this box interact with two detectors, a time of flight scintillator and a large surface energy loss PIN silicon detector [22]. Measurements at the object box establish incoming particle data, allowing for incoming particle identification. Just down the line, at the intermediate-image station, are two Tracking Parallel Plate Avalance Counters used in the tuning of the A1900 for use with the I beamline and S800. The target station is situated at the opening of the S800 dipole magnets, and for the course of e11037, it housed the LH_2 target and GRETINA.

After reacting with the target, the recoiled beam particles are collected by the dipole magnets and guided into the focal plane of the S800 where they are counted and measured. The first set of detectors in the focal plane are the Cathode Readout Drift Chambers (CRDC's), shown in Figure 2.5. They are spaced approximately 1 m apart and are used to calculate the trajectory of particles exiting the dipole magnets. Position measurements made by the CRDC's have a resolution of approximately 0.5 cm [23]. Ultimately, the CRDC measurements are used in connection with S800 inverse maps generated by a webserver operated by the NSCL to trace particle trajectories through the dipole magnets back to the target chamber for later analysis.
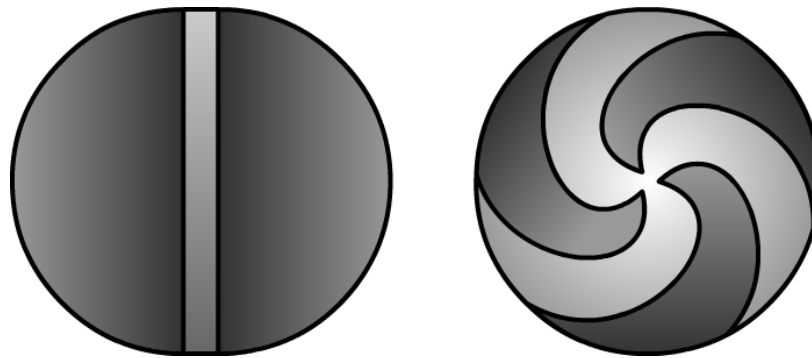
Figure 2.1: Comparison of K500 and K1200 coupled cyclotrons (right) to traditional cyclotron design (left). Charged particle trajectories are bent by static magnetic fields in the dark regions while particles are accelerated in the light grey regions. The NSCL design allows a longer acceleration path than traditional cyclotrons, yielding higher beam energies.
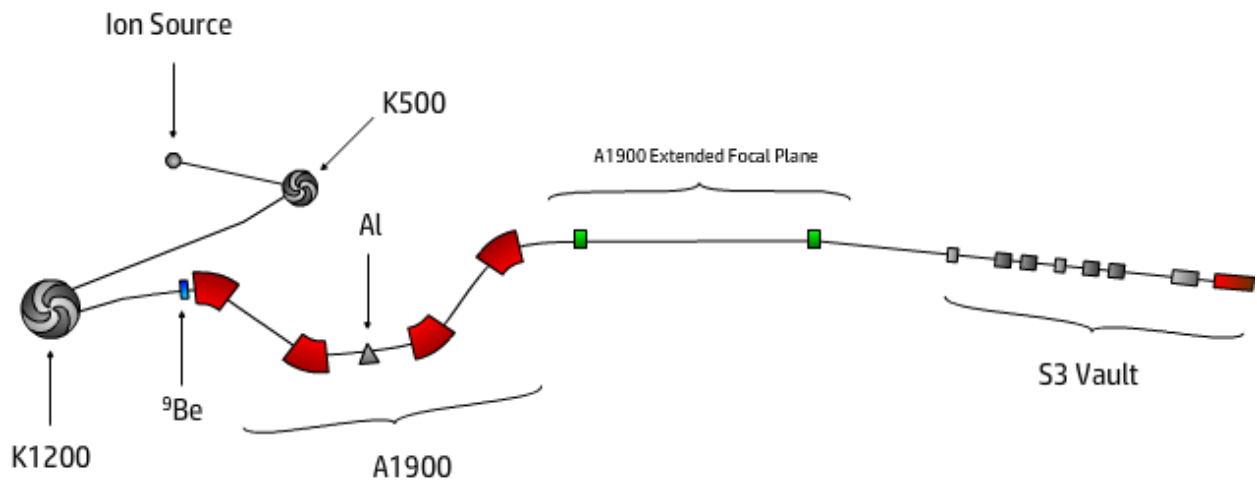
Figure 2.2: Dorsal view of NSCL beamline. Particles start at the ion source, accelerated through the K500 and K1200 coupled cyclotrons, fragmented by the ^{9}Be production target, filtered by the A1900 fragment separator, and guided downstream to the S3 vault.

9
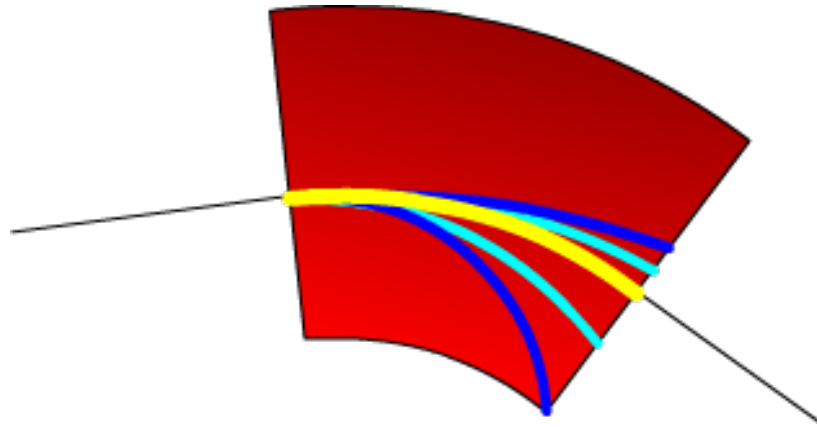
Figure 2.3: Diagram of an A1900 dipole magnet. As charged particles enter the magnet (left ray), their trajectory is bent into curved paths dependent on their charge state and momentum. Particles of desired charge and mass pass through the magnets into the beamline (yellow) while other particles escape the beamline (blue).
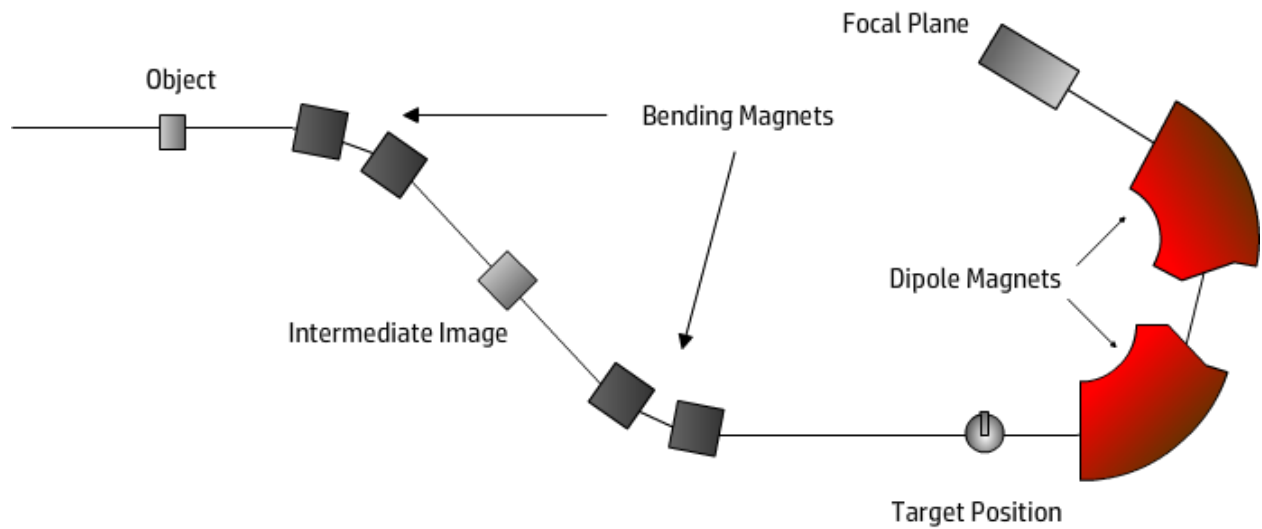
Figure 2.4: Diagram of instrumentation housed in the S3 vault. Particles enter at the object box, bent downward into the vault, react with the target, and pass through the S800 Spectrograph. The dipole magnets of the S800 sort the particle stream by charge and momentum for high resolution detection in the focal plane.
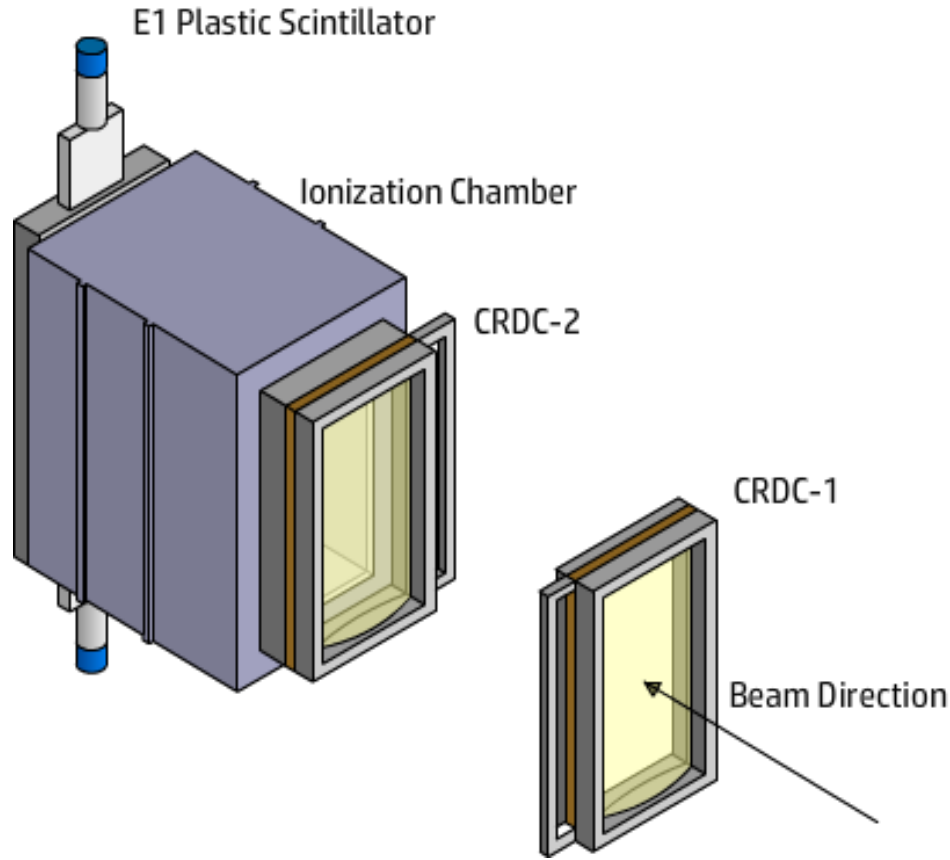
Figure 2.5: Diagram of instrumentation inside the S800 focal plane detector housing. The CRDC's detect particle position and trajectories, the Ionization Chamber detects energy loss of the particle stream, and the E1 plastic scintillator establishes a final time of flight measurement along with the S800 trigger.

The next detector in the focal plane is a 16-fold segmented Ionization Chamber used to measure energy loss of particles passing through the stacked parallel plate segments. Each segment is filled with 90% Ar and 10% CH_4 gas mixture, which reacts with the particle beam producing ions detected in the narrow anode-cathode gap. These energy loss measurements are coupled with the time of flight measurements in scintillators along the beamline, such as the aforementioned object box scintillator, to identify reacted nuclear species in the beam. A final plastic scintillator is installed after the Ionization Chamber, as well as a CsI(Na) hodoscope used to measure the total kinetic energy as well as different charge states of particles implanted in the sodium doped cesium iodide crystals [24].

2.3 GRETINA

The Gamma Ray Energy Tracking In-beam Nuclear Array (GRETINA) was installed at the target station of the S3 vault. GRETINA is the first stage development of a larger γ-ray detector system called GRETA (Gamma Ray Energy Tracking Array) that, when completed, will cover a total 4π angular coverage [25]. In the configuration available at the time of e11037, GRETINA consisted of 28 coaxially aligned hyper-pure germanium (HPGe) crystals, each segmented into 36 detection zones, shown in Figure 2.6 [26]. The aluminum support shell was designed to accommodate all of the eventual modules of GRETA, and currently allows a varied arrangement of the seven modules, each containing four crystals.

GRETINA functions in the same manner as most HPGe γ-ray detection systems. The crystal functions as a diode, and a reverse-bias is applied across the terminals of the crystal to produce a depleted zone inside the crystal, resulting in surface charge buildup on the contacts. The bias is tuned to produce a static electric field across the crystal such that electrons in the center of the crystal will drift toward the central contact and electron "holes" drift toward the segment contacts. As a photon passes through the crystal, it has a high probability of being absorbed by the crystal, either in a single interaction or through a succession of interactions due to Compton scattering. This photon will interact with the electron cloud of a Ge atom, and will cause one or more electrons to be ejected from the atom [27]. These photoelectrons are influenced by the static electric field to drift toward the central contact, and will quickly interact with nearby Ge atoms due to the short mean free path inside the Ge ejecting more electrons. These electrons drift, again, to nearby Ge atoms, and this repeated process produces a cascade of electrons [26]. At the same time, the holes left by the ejected electrons are quickly filled, producing a cascade of moving holes that drift toward the contact. The combined electron-hole cascades produce a current inside the crystal in between the central and segment contacts, which is measured and recorded. This current signal is integrated over time to measure the total charge excess produced from the incident photon. The charge excess is proportional to the energy of the incident photon, and depends on various characteristics of the specific crystal [28]. The proportionality is defined during calibration runs with the crystals.

While photons can deposit all of their energy in a single crystal in a single interaction point, the probability of this occurring is not 100%. Photons can undergo Compton scattering inside the crystal which results in a sequence of energies detected from a single incident photon. Furthermore,

these Compton scattered photons can move out of the original crystal into nearby crystals or simply into the open air. (See Figure 2.7) Photons of energy above the threshold $E_\gamma = 2m_{electron}c^2 = 1.022$MeV can produce an electron-positron pair in the Coulomb field of the Ge nucleus [29]. Older systems had high density plastic scintillators built around the Ge crystals that served as escape suppressors. Also known as Compton suppressors, signals produced by interactions with these high density scintillators were used as veto signals during the data acquisition, allowing γ-ray signals from within a single Ge crystal to be counted in the output γ-ray spectrum only when there is no associated suppressor signal. These suppressors were able to improve peak-to-total ratios but were a limiting factor on efficiency as the solid angle taken up by these shields sometimes equaled the solid angle occupied by the Ge crystals [30] [31].

The high degree of segmentation of the GRETINA crystals, along with the closely packed design, enables a unique feature in the field of γ-ray spectroscopy. The degree of segmentation allowed for the determination of the interaction points of the photons within the crystal by comparing the current signals produced in the segment contacts. In general, while a single detection zone will capture the full charge excess produced by the incident photon, surrounding segments will measure an image-charge signal. The shape and amplitude of these image-charge signals are dependent on the position of the interaction point relative to the segment the signal originated from [30] [32]. By using signal decomposition algorithms described in Reference [33], as well as comparing these signals to simulated basis signals, the position of the interaction point inside the crystal is determined. This interaction point along with the interaction points of events detected in coincidence with the original interaction point were used to track the path of Compton scattering events through the crystal, sometimes within the same segment, and across crystal boundaries. This tracking data is unique in its application as it does not require Compton suppressors, allowing for better usage of the solid angles available and improving γ-ray peak efficiencies. Positions of interaction points are measured to within two millimeters, which also enabled reconstruction of the original incident photon energies based on the angles between coincident interaction points [30].

For the present analysis, the raw γ-ray data was used, which included the raw Compton scattered events. The Compton reconstruction functionality was not used due to the use of GEANT γ-ray simulations that accounted for Compton scattering and GRETINA crystal geometry. The analysis did, however, benefit from the enhanced overall efficiency and improved peak-to-total ratios of the

newer GRETINA system over the originally planned SeGA system available at the NSCL. Paschalis, *et al*, performed initial testing on the performance of GRETINA, establishing the energy, noise, and time full width/half maximum resolutions of each crystal of the system, primarily using the 1173keV and 1332keV γ-rays of the ^{60}Co source. [30]. This yielded an average energy resolution of the GRETINA system of 2.22(14)keV, baseline noise of 3.82(25)keV, and timing resolution of 8.9(4)ns. In addition, they determined the raw peak efficiency of the array using the ^{60}Co source to be on the order of 7.5% for a γ-ray of energy 1332keV of multiplicity 1, and the raw peak-to-total ratio of the GRETINA system above a threshold of 200keV to be in excess of 0.4. More detailed descriptions of Ge detectors and Compton suppression systems can be found in Reference [34].

2.4 LH_2

The design of the Ursinus College LH_2 target was based on a similar device located at the RIKEN Nishina Center for Accelerator-Based Science. The plan for development of the target was produced by Dr. Lew Riley and Dr. Remco Zegers. The project was funded through grants written by Riley and supported by the NSF, and the target itself was built at the NSCL by Zegers. Installation of the target began with the reconfiguration of the GRETINA arrangement to accommodate the target and gas handling system. The arrangement used during e11037, as well as the additional two experiments performed with the target, is shown in Figure 2.8. All seven detector modules were installed in the northern hemisphere shell and the target beamline was installed with a 30° angle from the vertical, shown in Figure 2.9. Due to the angle of the support beam, a chain hoist was used to add support to the assembly upon installation, preventing torsion of the beamline and damage to the assembly.

The target assembly consisted of the target cell, cold arm, heater block, thermal diode sensors, radiation shield, and Sumitomo cryocooler, as shown in Figure 2.10. The gas handling system was installed as close to the target station as possible. It included the hydrogen source tank, gas reservoir, turbo and rotary pumps, three manometers, two flowmeters, and a plethora of valves arranged in the most efficient manner possible as shown in Figure 2.11. Not shown in either of these two figures is the helium compressor used by the Sumitomo cryocooler.

Due to the flammability of the hydrogen source, various precautions were put in place to prevent explosive damage to the target, the beamline, and GRETINA. As part of these precautions,
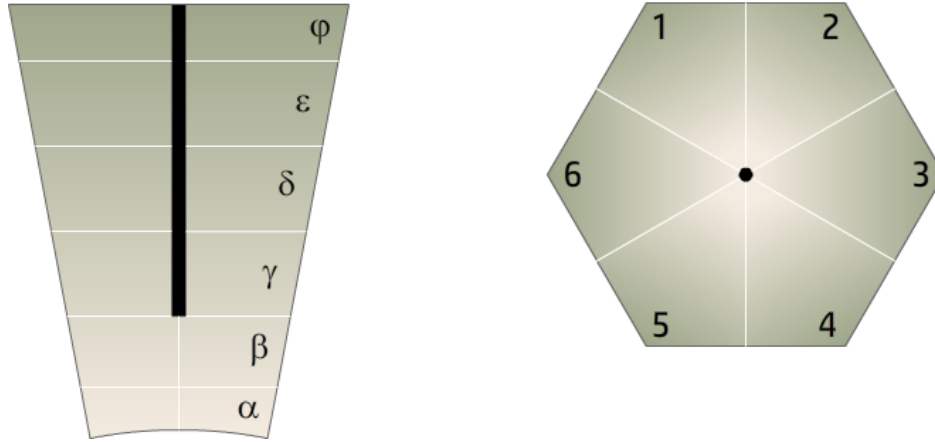
Figure 2.6: GRETINA crystal segmentation. Each crystal is segmented into six longitudinal and six transverse segments, creating 36 separate detection zones. This high level of segmentation allows for position resolution of an event within two millimeters.
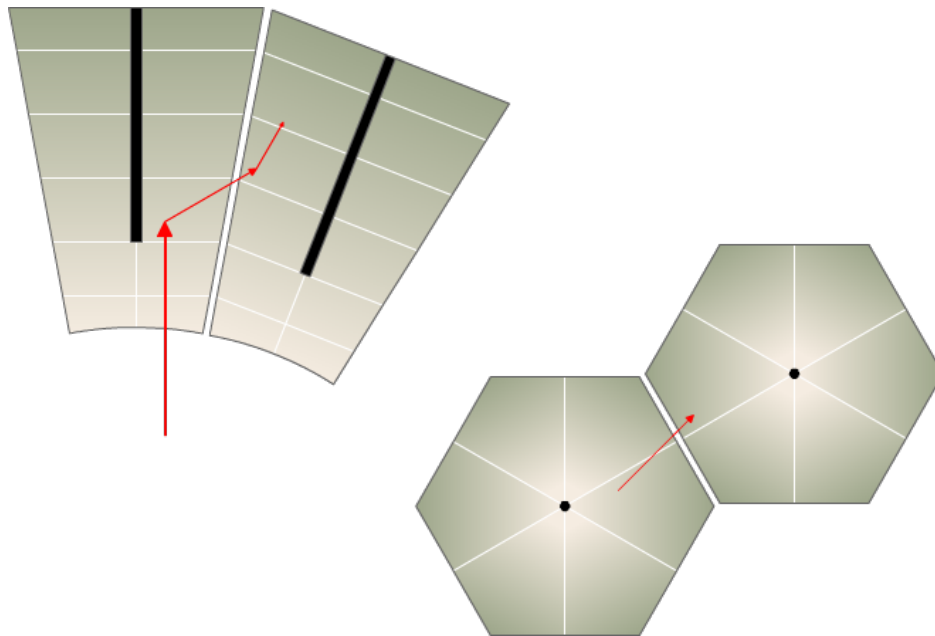
Figure 2.7: GRETINA crystals detecting an incident γ-ray. In some cases, the entire energy of a single incident photon will be deposited into a single crystal detection zone, but often the γ-ray will undergo Compton scattering and pass out of the crystal before the energy of the entire incident γ-ray is detected. The GRETINA data farm is capable of reconstructing the total single photon crystals based on timestamps, detection zones, and Compton angles.

(a) Diagram   (b) Photo taken by author
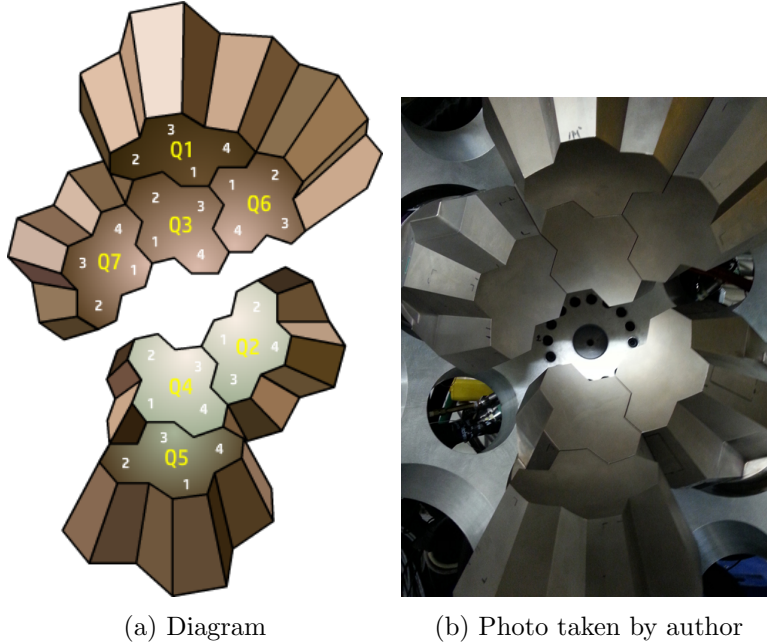
Figure 2.8: Arrangement of the GRETINA Crystals during e11037. This arrangement was made to accommodate the installation of the liquid hydrogen target and gas handling system. All but one of the detectors used the standard output box; the Q5 module was attached with a "Fishtail Radial" box as space below the deck for the gas handling system installed was limited.
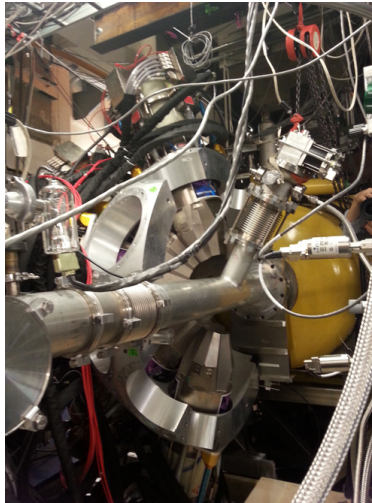
Figure 2.9: Installation site of LH_2 target inside its beamline housing at the center of GRETINA. The hoses and cables in the right frame of the image were from the gas handling system installed in close proximity to the target. Photograph taken by author.
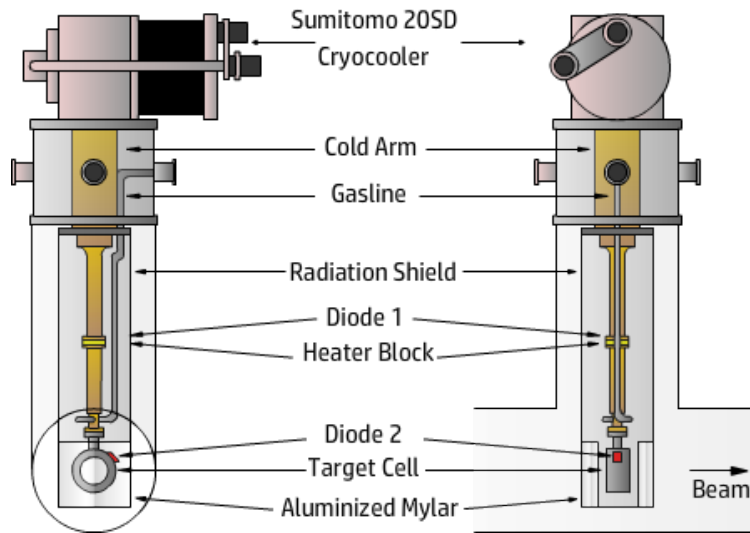
Figure 2.10: Design of the LH_2 target, based on design by Ryuto, *et al*, at RIKEN Nishina Center for Accelerator-Based Science. Diode sensors were connected to ports similar to the hydrogen gasline port.
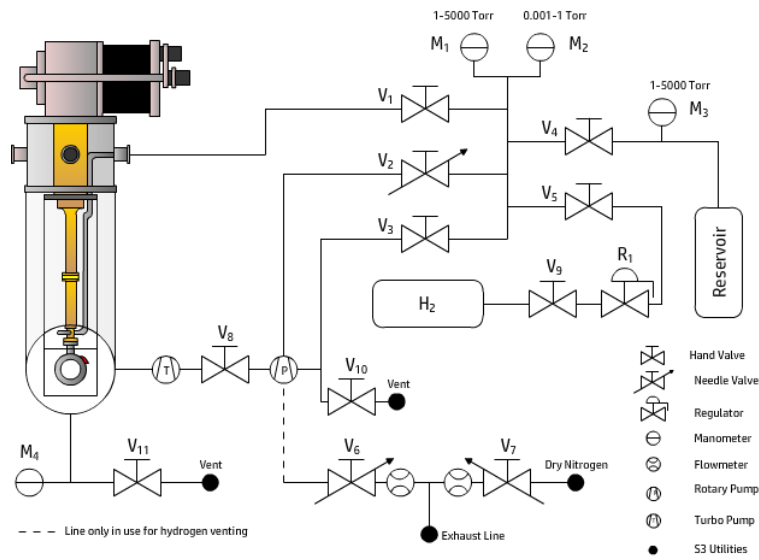
Figure 2.11: Diagram of the LH_2 target gas handling system. The installation process was extensive, as was the testing phase to ensure stability in the Kapton windows.

extensive training was required of target operators, including the author. Exhaustive testing of the target cell was performed after installation of the target to ensure proper operation during the three experiments performed using the LH_2 target during this run.

During the first two experiments, e11035 and e12016, there was an issue that arose with the target cell temperature. To maintain adequate fluid levels, and ensure the liquid hydrogen did not boil, the temperature of the target was manipulated by the cryocooler and heater block to set it at approximately 18K. However, fluctuations of the temperature were seen in amounts of between 0.5K and 1.0K above and below the set temperature. It was believed that blackbody radiation from the dipole magnets of the S800 spectrograph, in very close proximity to the target, was responsible for the variance in the target cell temperature. Aluminized mylar was placed over the openings of the radiation shield to further reduce radiation exposure of the target for the course of the third experiment, e11037. This remedy appeared to work as the temperature of the target cell remained at 16K with fluctuations well below 0.2K for the duration of the liquid runs of e11037.

E11037 ran for approximately 131 hours, including six hours of basic calibration runs along with 17 hours of empty cell runs. Once the target was installed and beamline under pressure, the cell could not operate completely empty as the Kapton windows could easily be damaged. An empty cell was approximated by running the cell at around 80-90K, leaving the target cell empty of liquid but still filled with gaseous hydrogen under pressure just above 1 atmosphere. In total, roughly 114 hours of liquid hydrogen runs were recorded by the GRETINA-S800 detector system. As mentioned above, the temperature of the target was stable at 16K and pressure was maintained at just above 1 atmosphere to prevent damage to the Kapton windows in the unlikely event of sudden decompression of the beamline. Due to the plastic nature of Kapton, the cell windows bulged in the vacuum space of the beamline roughly 2.3mm and held at that value through the entirety of e11037.

2.5   Data Acquisition

During the experiment, secondary beam particles passing through the target, including particles reacting with the target, were detected by the S800 Spectrograph. The particles were sorted by charge state and mass by the dipole magnets, and measured by the detectors in the focal plane.

Each S800 event included information from all of the detector systms along the S3 vault, as well as additional information from the A1900 extended focal plane for use in particle identification.

γ-rays released by reactions with the target, as well as released by natural decay of particles in the beam and in the target hall itself, were measured by GRETINA. As data was recorded, basic γ-ray energies were reconstructed by the GRETINA data farm, establishing energies as well as GRETINA event timestamps. All GRETINA events were detected in coincidence with S800 events using the timestamp system linking the two detectors and were written to disk. The timestamp correlation patterns had been previously established as a function of beam velocity and dipole magnet rigidity settings when GRETINA was initially installed in the S3 vault. The experiment accumulated more than 800GB of data, including the raw data acquired and the initial correlation sort performed by the data farm. The NSCL kept records of the experiment for the event of data recovery while at least two copies of the data set were initially taken from the experiment, one for Lew Riley and his undergraduate students at Ursinus College and one for the author.

2.6   Particle Identification

Apart from GRETINA, the S800 Spectrograph system is a powerful tool used for particle identification (PID). As mentioned earlier, the S800 Spectrograph is a high resolution and large acceptance mass spectrometer. It is unique to its class of detector in the fact that it is mounted in the S3 vault frame capable of being rotated around a pivot point, referred to above as the target position. The rest of its operation is very much the same as other mass spectrometers, sorting the particle stream by charge and mass so that different charge and mass states are easily resolved. This allows very accurate measurements of energy loss of particles, relating to the mass state of the particle in the system. After exiting the Ionization Chamber, the particles triggered the E1 plastic scintillator, establishing the event timestamp.

Also mentioned earlier, detectors were installed at the object of the S800. The plastic scintillator at this box was used to establish time of flight measurements of particles passing through it. Timestamps of these time of time of flight measurements were correlated with the E1 scintillator trigger. These timestamps were, of course, made in coincidence with energy loss measurements in the Ionization Chamber, and thus downstream outgoing PID spectra were generated plotting energy loss versus time of flight, shown in Figure 2.13.

Incoming PID is established in a similar manner, except that for the course of e11037, the energy loss was measured by the silicon pin diode at the object box while the time of flight measurements were taken as a subtraction between the time of flight at the object box plastic scintillator and the A1900 extended focal plane plastic scintillator. The upstream incoming PID spectra were generated plotting energy loss versus time of flight, shown in Figure 2.12.

Personnel at the NSCL were able to identify the primary constituent of the beam as ^{47}K, shown in both incoming and outgoing PID. The identification was made by relating energy loss versus time of flight with the reference frequency of the cyclotrons. This identification allowed the subsequent identification of the incoming and outgoing ^{48,49}Ca and ^{50}Sc particles passing through the target, either simply or by elastic and inelastic reaction with the target.

In conjunction with GRETINA, these PID measurements are a very powerful tool. Sorting gates can be drawn in the PID spectra around areas of interest, such as ^{48,49}Ca and ^{50}Sc, and the data set can be sorted focusing on timestamps of events inside the gates. In total, approximately 39 million ^{49}Ca particles, 4.7 million ^{48}Ca particles, and 1.6 million ^{50}Sc particles were generated during the liquid cell runs of the experiment, based on the PID gated global trigger events. GRETINA events in coincidence with the S800 events inside the gates were detected in coincidence with the identified nuclear species, allowing for identification of γ-rays with these nuclei. In the case of the analysis presented further on, the task of sorting the data using incoming and outgoing ^{48,49}Ca and ^{50}Sc generates γ-ray spectra associated with inelastic reactions of these nuclei with the proton target. Various other reactions are possible, depending on the assignment of the outgoing PID gates, but inelastic reations are of interest in this analysis.
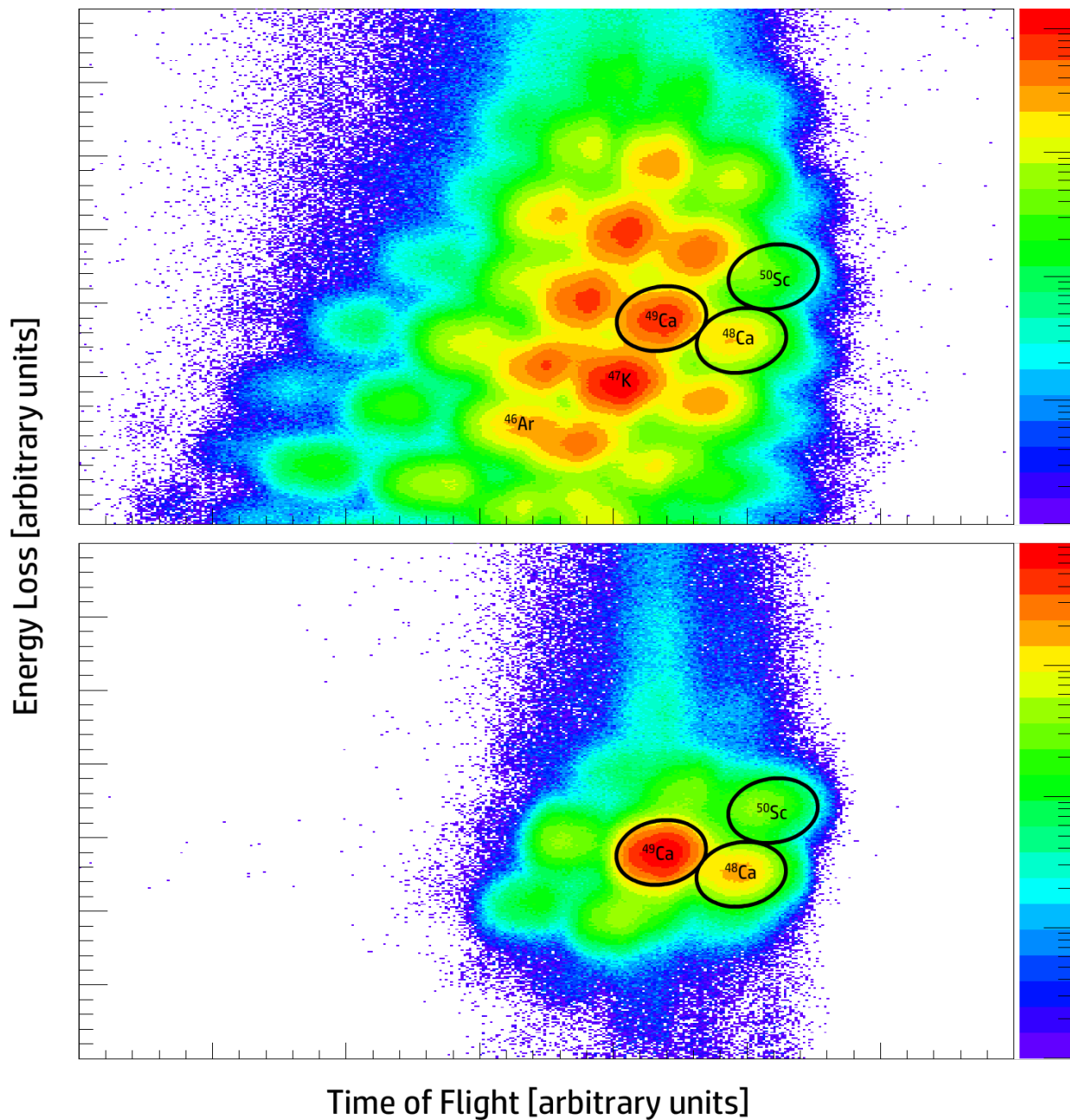
Figure 2.12: Incoming particle identification (PID) spectra used by NSCL personnel and users for analysis of GRETINA-S800 data. Top panel is the full spectrum while bottom panel is a sorted spectrum focused on ^{48,49}Ca and ^{50}Sc.
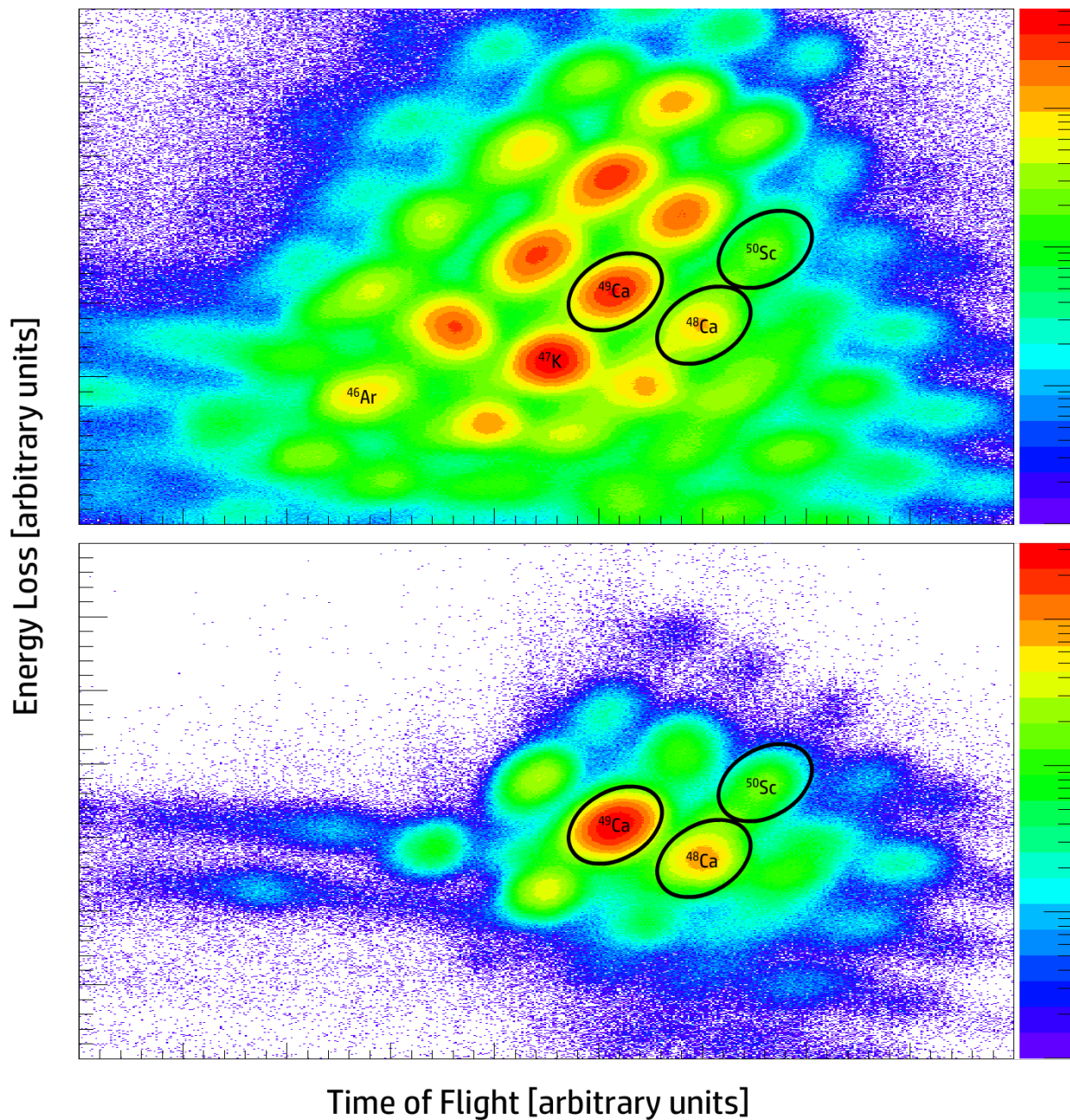
Figure 2.13: Outgoing particle identification (PID) spectra used by NSCL personnel and users for analysis of GRETINA-S800 data. Top panel is the full spectrum while bottom panel is a sorted spectrum focused on ^{48,49}Ca and ^{50}Sc.

CHAPTER 3

ANALYSIS OF DATA

3.1   Initial Analysis and Findings

3.1.1   Calibrations of GRETINA-S800 Data

The first few steps to analyzing the data from e11037 were to calibrate the analysis software ROOT, developed by CERN, and the sorting package GRROOT, written and supported by personnel at the NSCL [35]. The process of calibration began with creating initial PID on ^{46}Ar. This nucleus had been previously explored by Lew Riley and was used as an example case for calibrations. The gates were drawn around the regions identified in the PID spectra as the incoming and outgoing ^{46}Ar, shown in Figures 2.12 and 2.13. After the initial gates were drawn, the Ionization Chamber data was calibrated first. Using the subroutine ICCAL provided in the GRROOT package, each of the gated channels of the ion chamber were matched to a single channel, normalizing all of the ion chamber data. Due to these changes, the PID spectra changed, shifted due to the calibrations, and so new gates where drawn to accommodate the changes. With these new gates, the next step was to calibrate the CRDC pad data. This step consisted of an iterative process, using a similar procedure to the ion chamber calibration. The GRROOT subroutine PADCAL calibrates all of the pads relative to a single user-defined pad. In comparison to the Ionization Chamber calibrations, CRDC pad calibrations aren't absolute as each pad is set relative to another. However, by repeating the process iteratively, the calibration converged on a single set of settings. After the base normalization calibration was finished, the CRDC position settings were also calibrated. During runs 22 and 23, masks were placed on each of the CRDC's, producing a pattern in the measured data. By aligning the measured pattern with the physical specifications of the masks, the CRDC's were calibrated yielding position accurate data. Once this was done, a final calibration was done to the ion chamber position data. Energy loss measured in the ion chamber is position dependent, corrected by the relation

$$E_{corrected} = E_{measured} \cdot e^{p \cdot (x - x_0)} \tag{3.1}$$

A script file included with GRROOT was used to generate a gated spectrum of the ion chamber energy loss versus x_0. This spectrum was fitted using the above equation, yielding the parameter p which was factored into the settings files. After these steps to calibrate the Ionization Chamber and CRDC data, minor timing corrections were performed on all of the data by modifying parameters in the settings files to align the timing spectra to a straight line.

Once all of these calibrations were performed, one more calibration was needed for each individual reaction to be studied, namely inelastic reations of ^{48,49}Ca and ^{50}Sc. Using settings of the S800 magnets, along with the proton, neutron, and total nucleon number of the incoming nucleus of interest, an inverse map was generated by using the S800 Spectrograph Inverse Map Server located on the NSCL website [36]. These inverse maps were used in conjunction with PID gates for each nuclear reaction of interest to sort the data. This sort calculated the trajectories of the nuclei, generating the dispersive and non-dispersive angles of particles exiting the target. The mean values of these two spectra were factored into the settings files for each nuclear reaction of interest to improve the reliability of calculations performed further on.

3.1.2 S800 Momentum Acceptance

Full analysis of the data started with the ^{48}Ca nucleus as it is a mostly stable nucleus that has been well studied. However, an issue with the gated data for this nucleus was discovered. The kinetic energy profile for ^{48}Ca, generated from the energy loss of each particle relative to the angle at which it entered the S800, did not have the shape that was expected. In general, it is expected that particles scattering off the proton target would yield a Gaussian distribution, allowing for a range of possible final momenta, which is related to the kinetic energy profile generated from the data. In the case of ^{48}Ca, shown in Figure 3.1, there is a relatively clear cutoff from the expected distribution. This cutoff represents a loss of data during the experiment as it demonstrates that a portion of the ^{48}Ca particles were not detected by the S800 due to its momentum acceptance. Figure 3.2 demonstrates this momentum acceptance. As particles enter the dipole magnets of the spectrometer, their trajectories are curved into a circular path with radii that depend on the particle momentum (mv), charge (Z), and strength of the dipole magnetic field (B) by the relation

$$R = \frac{mv}{ZB} \tag{3.2}$$

In the case of ^{48}Ca, the paths of the ions in the S800 were bent too strongly and a portion of the ions went undetected by the S800 trigger system, as demonstrated by Figure 3.2. This loss of triggered S800 events corresponded to an inaccurate count of outgoing ^{48}Ca particles. This loss of S800 events also corresponded to a loss of GRETINA events. This was a correctable issue, as will be described later, however it was decided to proceed with the analysis of ^{49}Ca nucleus as there was no discernable cutoff in its kinetic energy profile (See Figure 3.1).

3.2 γ-ray Yields

3.2.1 ^{49}Ca

The first step in analyzing the data yields for inverse kinematic $^{49}Ca(p, p')^{49}Ca'$ reactions was to first determine whether the gating system was sorting the data properly to produce the γ-ray spectrum associated with this reaction. After performing an initial sort of the data set, the resulting Doppler corrected γ-ray spectrum appeared to contain most of the known γ-rays associated with low-lying energy levels of ^{49}Ca. The gated, Doppler corrected γ-ray spectrum for the inelastic proton scattering by ^{49}Ca is shown in Figure 3.3.

After confirming the efficiency of the gates, the process of generating integrated γ-ray yields for each γ present in the spectrum began. A ROOT script was written to fit the measured, Doppler corrected γ-ray spectrum using background measurements and GEANT simulations. Establishing the appropriate parameters to run the simulations was an extensive process.

The first phase started with determining a linear relationship between the kinetic energy profile of the beam and the dispersive angle measurements in the intermediate image PPAC detectors in the empty cell runs. This relationship was used as a template to convert the dispersive angle measurements into kinetic energy profiles. This was useful as it was not possible to measure the incoming beam kinetic energy profile during the liquid cell runs. The shape of the incoming kinetic energy profile was used to drive realistic simulations. The first set of simulations generated were ion simulations used to fine tune the parameters of the γ-ray simulations.

One such parameter in the simulation macro files was the target bulge value. By varying this parameter in short ion simulations, an accurate value for the target thickness was determined by matching the mean value of the actual and simulated kinetic energy profiles. In addition, the kinetic energy parameter of the incoming ^{49}Ca particles also had to be set properly using the physical
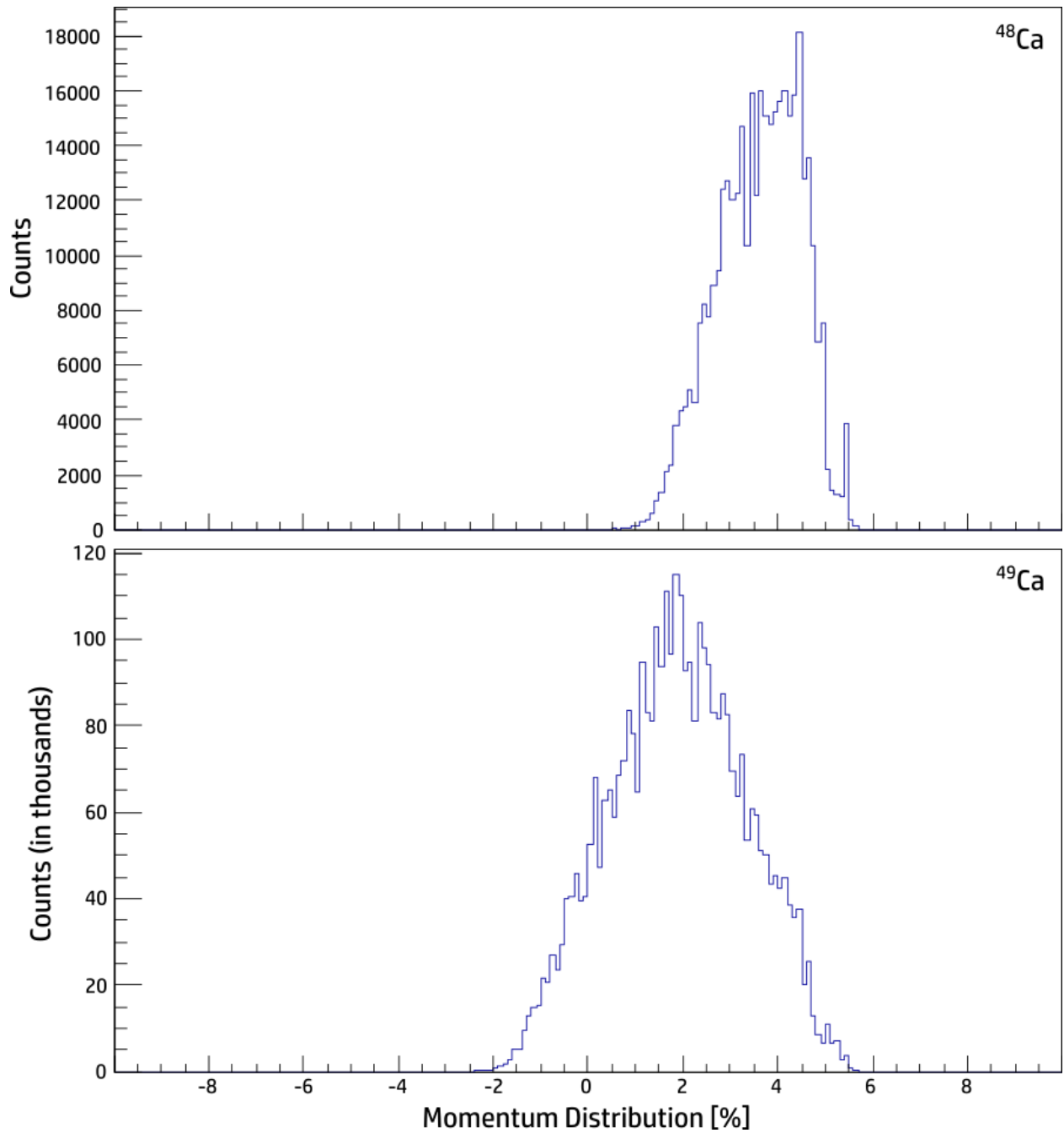
Figure 3.1: Kinetic energy profiles of ^{48}Ca (upper panel) and ^{49}Ca (lower panel). The spectrum for ^{48}Ca shows a clear cutoff due to the momentum acceptance of the S800 where the ^{49}Ca spectrum does not.
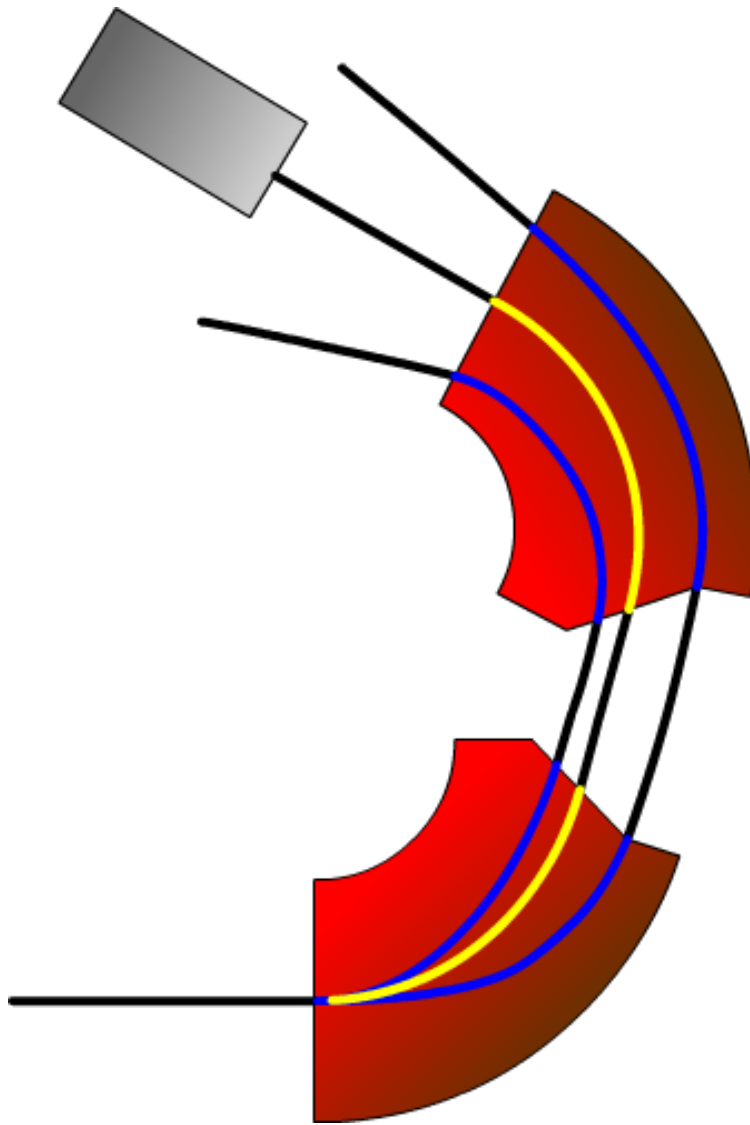
Figure 3.2: Diagram demonstrating momentum acceptance of the S800 spectrograph. As the charged particles enter the static magnetic fields of the dipole magnets (lower beam), their trajectories are bent into circular paths with radii determined by charge state and momentum by Equation 3.2. The yellow line represents paths of particles that make it through the momentum acceptance of the S800 while blue lines represent lost particles.
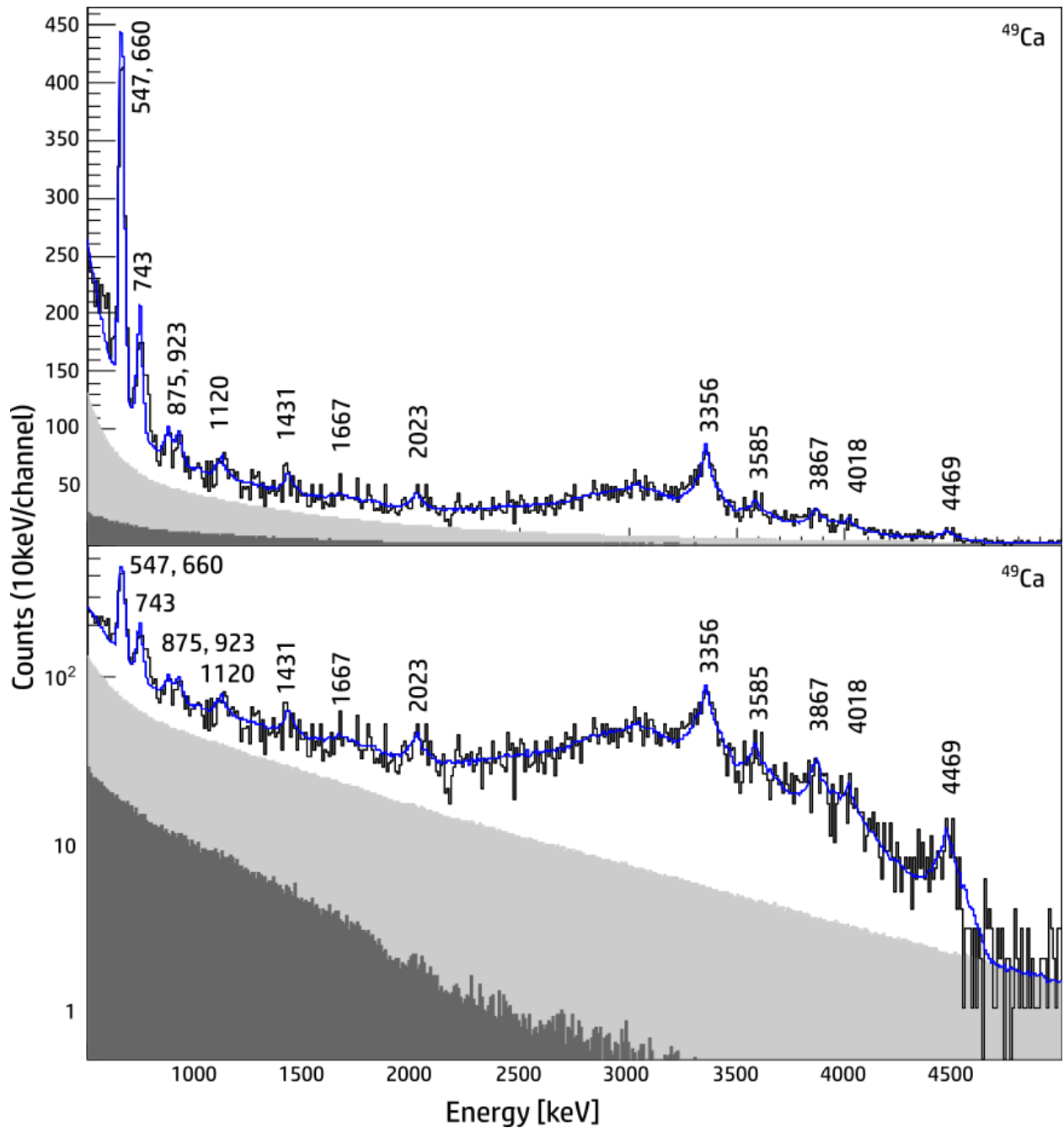
Figure 3.3: Gated and Doppler corrected γ-ray spectra for ^{49}Ca. The bottom spectrum is the logarithmic scale of the top spectrum. The measured spectra are shown in black while the fitted function defined by Equation 3.3 is shown as in blue. The background measurements are shown by the grey areas; prompt in light gray and non-prompt in dark gray.

calculator of the program LISE++. Once all of these parameters were established, simulations were performed for each γ-ray of interest.

These simulations calculated the probability of detecting a particular γ-ray, 4016keV for instance, out of 10^6 events and constructed the theoretical, Doppler corrected γ spectrum. These calculations also included the probability of Compton scattering inside the target, the radiation shielding, beamline, and crystals of GRETINA. It is for this reason that the analysis method did not use the enhanced Compton tracking data generated by GRETINA. The simulated γ spectra essentially accounted for the efficiency of the array at large. By fitting each simulated γ-ray spectrum along with a background measurement to the gated, measured γ-ray spectrum, accurate counts for each simulated γ-ray could be extracted from the output of the ROOT script.

The fitting script used within the framework of the ROOT software operates on a rather simple basis. The code takes in as input the measured, gated γ-ray spectrum, a background γ-ray spectrum, and all of the simulated γ-ray spectra generated. It initializes a function with a shape of the form

$$f(x) = e^{(p_0 + p_1 x)} + e^{(p_2 + p_3 x)} + p_4 S_{bkgd}(x) + p_5 S_{\gamma 1}(x) + p_6 S_{\gamma 2}(x) + \ldots \tag{3.3}$$

where x is the bin number, p_i are variable parameters, and all of the functions $S_i(x)$ are the bin contents at x of the γ-ray spectrum inputs into the code. The function $S_{bkgd}(x)$ was specific to the background measurement spectrum. The ROOT code fit the parameters in the above equation channel by channel so that the final fitted function matched the measured, gated γ-ray spectrum as closely as possible.

The code is capable of fitting in both the laboratory frame as well as the projectile frame, depending on the input spectra. The two exponential terms of Equation 3.3 are able to approximate the background γ-rays detected in coincidence with incoming and outgoing ^{49}Ca. However, there is a portion of the background, the non-prompt component of it in fact, that is not accounted for by the exponential functions. This was dealt with by the inclusion of the $p_4 S_{bkgd}(x)$ term in the fitting function. In the projectile frame fit, this parameter was fixed, but in the laboratory fit frame, it was the only background parameter allowed to vary. Using an iterative process, fixing parameters from one frame to another, the parameters p_0, p_1, p_2, p_3, and p_4 converged on a specific set of parameters. The final value of p_4 was fixed in the projectile frame fitting to generate the final set of parameters p_5 and beyond. The values of these parameters, when scaled with the number

29

of simulated events, represented the counts of photons released in the experiment and detected by GRETINA, either as the full energy γ-ray or as a secondary Compton scattering event. It is important to note that the fitting of the p_4 parameter did not significantly change any of the γ-ray counts. Comparing the counts fitted with the final p_4 value and counts fitted with the parameter set to zero, the counts varied by less than 5%, which was well within the statistical uncertainty of the fits generated by the fitting code.

One issue to address with the fit is the resolution to use in the fitting process. The sorting code GrROOT is capable of sorting the histogram spectra into various resolutions. While resolutions of 1keV/channel are available, these fine resolutions are too noisy to gain physical information from. Larger bin sizes enable better peak to noise ratios, but there is a limit to this effect as resolutions larger than 20keV/channel blur together closely spaced γ-rays. One way to address this issue is to analyze how the fits change as the resolutions change.

Scanning across resolutions from 1keV/channel to 20keV/channel gave insight into the stability of the fitting process for each γ-ray. Low percentages of the standard deviation relative to the average counts in a particular γ-ray indicated that the fit was only weakly dependent on the binning size, and of course, higher percentages indicates a strong dependence. This effect was not always going to be the same for all γ's to be fitted as larger peaks are more likely to have a weaker dependence. This does not, however, indicate that smaller peaks specifically have strong dependence. In fact, as various simulation settings and data corrections were applied these percentages became smaller. This was a strong indicator that, from a statistical standpoint, the count fits were actually converging on accurate values represented in the data from e11037. It was decided that percentages less than ten percent were reasonable to have strong confidence in the accuracy of the fits, especially when the standard of deviation sat well within the statistical uncertainties of the fits.

Further analysis was performed using the γ-ray yields from this point to generate preliminary findings on the ^{49}Ca nucleus. However, for the purpose of this dissertation, these preliminary analyses were not included here as errors in the initial analysis were discovered. These errors were eliminated when ^{49}Ca was analyzed again using a slightly altered procedure designed to account for the S800 momentum cutoff encountered in the ^{48}Ca data.

3.2.2 ^{48}Ca

Dealing with the loss of data acquired by the S800 Spectrograph was not a simple task. Given the Gaussian nature of the distribution of the kinetic energy profile, one might consider using an extrapolation method to complete the distribution for ^{48}Ca. However, this would not have been a useful endeavor as the loss of S800 events also included loss of GRETINA events detected in coincidence. Simple extrapolation wouldn't have reconstructed the missing GRETINA data, and scaling the already available GRETINA data by a factor consistent with the extrapolation would have been in error. The reason for this was that the kinetic energy profile includes elastic and inelastic data, but they are not evenly distributed across the entire distribution. Application of extrapolation from the profile would have skewed the GRETINA data, biasing it toward either the elastic or inelastic data. Since the focus of this analysis is on inelastic reactions with the proton target, a bias in either direction would have produced inaccurate counts concerning the inelastic reactions.

Fortunately, a procedure was devised to account for this cutoff without introducing a bias and integrated into the analysis process. The process started very much in the same manner as the ^{49}Ca nucleus, verification of the gating system. The initial sort performed on the data set using the incoming and outgoing ^{48}Ca generated a γ-ray spectrum containing previously known γ-rays associated with ^{48}Ca. When compared to the spectrum of ^{49}Ca, it is clear that there are no significant contributions from either nucleus in the gated γ-ray spectrum of the other (See Figure 3.4).

The next step differed from the original method used on ^{49}Ca. Instead of using the relationship between the kinetic energy profile of the beam and the dispersive angle measurements in the empty cell runs to generate the incoming beam kinetic energy profile of the liquid cell runs, the new method simply used the kinetic energy profile of the empty cell runs to drive the GEANT simulations. Lew Riley and his undergraduate students ran several test cases and discovered little difference between using the energy profile of the empty cell runs and the previous method used.

Also, other parameters, such as the target bulge, were no longer in need of modifying as all of the beam products entered into such a small beam spot on the target that any variance in the target bulge between nuclei analyses would probably be negligible. As in the ^{49}Ca case, the kinetic energy parameter was for the incoming ^{48}Ca particles was also set using the LISE++ physical calculator.
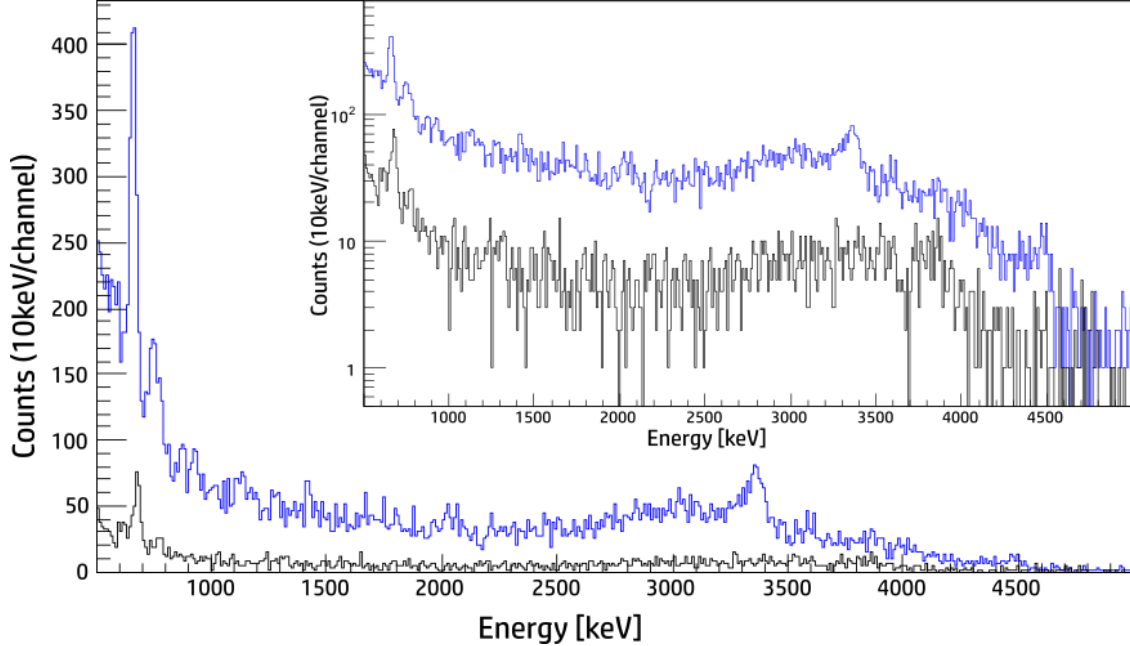
Figure 3.4: Comparison of ^{48}Ca (black) and ^{49}Ca (blue) gated and Doppler corrected γ-ray spectra. Inset graph is logarithmic scale of the outer spectrum.

Ion simulations were performed, focusing on modifying the kinetic energy parameter until the mean of the simulated kinetic energy profile was matched to the measured outgoing kinetic energy profile of the beam during the liquid cell runs. All of the parameters set were transferred to the macro files to run γ-ray simulations for ^{48}Ca. Also, from the output of the ion simulations, the average velocity of the reaction particles was established to perform a more accurate Doppler correction of the data.

Application of the simulations unaltered in the fitting algorithm in the same manner as the first ^{49}Ca analysis, the fitting code would have generated parameter fits far lower than were actually detected as the simulations didn't account for the loss of triggered S800-GRETINA coincidence events. To deal with this, the simulations for ^{48}Ca generated not only γ-ray spectra, but also an additional spectrum plotting the kinetic energy profile of the recoiled ^{48}Ca versus the γ-ray energy released from the recoiled particles. This specific spectrum, referred to as the acceptance spectrum, was used in the fitting code in conjunction with an acceptance cut file generated from a simulation of the momentum acceptance of the S800 performed by Lew Riley. As shown in Figure 3.5, the cut

file essentially eliminated a portion of the γ-ray counts from the simulated γ-ray, specifically γ-rays from particles that the simulations predicted were lost due to the S800 momentum acceptance. When the modified γ-ray spectra were folded into the fitting code, the fitted parameter outputs were more representative of γ-ray counts actually detected by GRETINA in coincidence with the detected ^{48}Ca particles. The measured γ-ray spectrum of ^{48}Ca, along with the fit function, is shown in Figure 3.6.

The ^{48}Ca fits were run through the stability test used on the ^{49}Ca data, and all passed with reasonable certainty of stability. The uncertainties of each γ-ray measured in ^{48}Ca were larger on average than those found in the ^{49}Ca fits, but this is understandable given the lower counts of ^{48}Ca particles versus ^{49}Ca particles passing through the target. The γ-ray counts measured were used in generating cross sections associated with the ^{48}Ca inverse kinematic proton scattering reactions explained in a later section.

3.2.3 ^{49}Ca Revisited

Despite having no visually discernible S800 cutoff in the kinetic energy profile, ^{49}Ca was analyzed again using the same S800 acceptance method for the ^{48}Ca. This was primarily done as an additional verification of the analysis method, testing the difference between using a calculated incoming kinetic energy profile of the liquid cell beam versus using a measured kinetic energy profile of the empty cell beam as the driving function in the γ-ray simulations. Steps identical to the ^{48}Ca procedure were performed, and γ-ray yields generated were similar to the original analysis method. In the fitting process, an acceptance cut ratio was generated by integrating the modified simulation spectrum and dividing it by the integrated original simulation spectrum. This ratio was on average 0.78 for the ^{48}Ca nucleus, but for ^{49}Ca, it sat close to unity, but not exactly at a value of 0.95. This indicates that there was a small cutoff due to the S800 momentum acceptance. This small variation accounts for the minor differences between the γ-ray yields generated by the two analysis methods.

The newer ^{49}Ca fits were run through the stability test, and all of the γ-rays were reasonably stable, except for the 151keV γ-ray. As shown in Table 3.1, as the bin size increased the measured counts also increased. In all of the other γ-rays, this behavior wasn't present. In fact, there was no discernible repeating pattern among the other sets of parameters, not to mention variances far smaller than the ones seen in the 151keV parameter. The reason behind the behavior of the counts
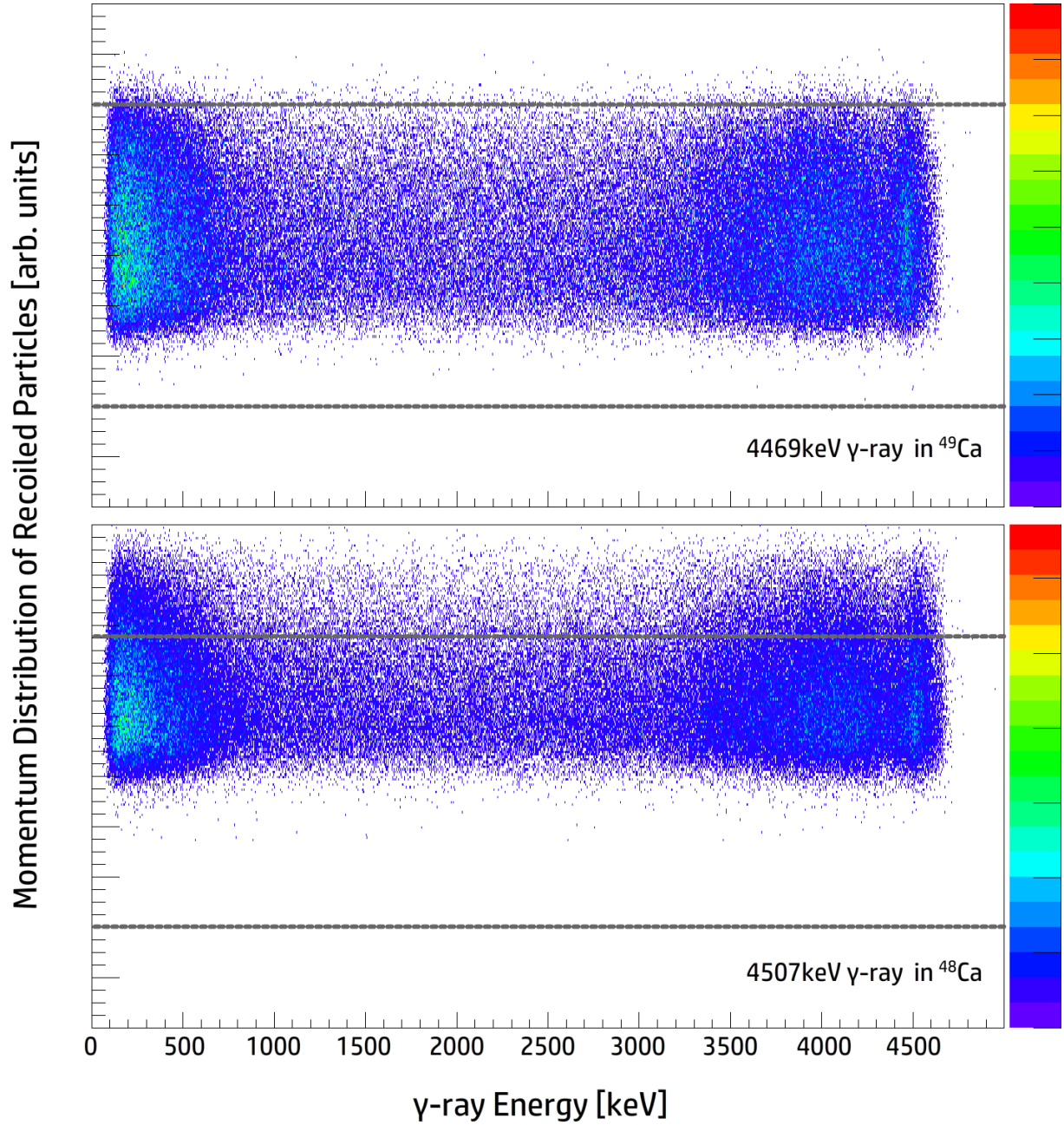
Figure 3.5: Acceptance spectrum built from GEANT simulations, plotting kinetic energy profile of recoiled particles versus scattered γ-ray energies detected. The gray dashed lines indicate the momentum acceptance of the S800 spectrograph as particles with momentum and charge state of particles inside the lines made it into the focal plane of the S800.

Figure 3.6: Gated and Doppler corrected γ-ray spectra for ^{48}Ca. The bottom spectrum is the logarithmic scale of the top spectrum. The measured spectra are shown in black while the fitted function defined by Equation 3.3 is shown as in blue. The background measurements are shown by the grey areas; prompt in light gray and non-prompt in dark gray.

is explained by the fact that the 151keV γ-ray sits on the rising ridge of the background, as shown in Figure 3.7. This was accounted for by averaging the measured counts in this peak, and setting the uncertainty for this γ-ray as the difference between the average and the extremum of the measured counts. This particular γ-ray only partially passed the first stability test due to the fact that the first test only used ranges of 3keV/channel to 10keV/channel. The extention of the test to 1keV and 20keV/channel was made during the analysis of the ^{48}Ca data.

3.2.4 ^{50}Sc

In addition to the analysis on ^{48}Ca and ^{49}Ca, it was also decided to perform an analysis on ^{50}Sc that was contained in the secondary beam of e11037. Little is known about this short lived nucleus, in fact most, if not all, of the γ-rays detected during e11037 for this nucleus had not previously been observed. Inverse kinematic proton reactions, however, are capable of generating octupole vibrations given the relatively high energy of the beam products in e11037.

The method used to analyze ^{50}Sc was the same method used to account for the S800 momentum acceptance, however this process was significantly stunted in execution relative to the other two nuclei studied. In the case of ^{48,49}Ca, the γ-rays of interest were already known, for the most part. The simulation macros were written using already known values of the γ-ray to be simulated. For the previous three analysis runs, the γ-ray parameters were set based on their relative presence in the total gated γ-ray spectrum and their assignment found in literature. In fact, the 151keV γ-ray in ^{49}Ca had been mistakenly assigned as 156keV based on information found in literature but was discovered during the stability test in the second round of analysis on that nucleus [37]. However, as mentioned, the γ-ray energies associated with negative parity states in ^{50}Sc were not previously known to the author at the time of the analysis and thus were not available to enter into γ-ray simulations.

Establishing all of the other parameters of the γ-ray simulations was a simple process, but defining the γ-ray energy parameter required studying the total gated γ-ray spectrum in very fine detail. Starting with energies around 200keV, peaks were identified in the full γ-ray spectrum using a wide range of resolutions. Several low energy peaks were identified in the 400-1000keV range, with a few higher energy peaks as well. The energies were defined with uncertainties of about 5keV given the low statistics in the spectrum, and were written into γ-ray simulation macro files to run. In some cases, multiple macros were written and simulated for a single peak to more accurately

Table 3.1: Stability Test for the 151keV γ decay in ^{49}Ca. Bin sizes are listed in keV/channel.

Bin Size	Counts	Uncertainty
1	7010	828
2	7034	831
4	7285	735
8	9055	811
10	8698	986
12	8606	767
16	9295	828
18	10215	881
20	12024	945
Average	8802	846
Deviation	1635	
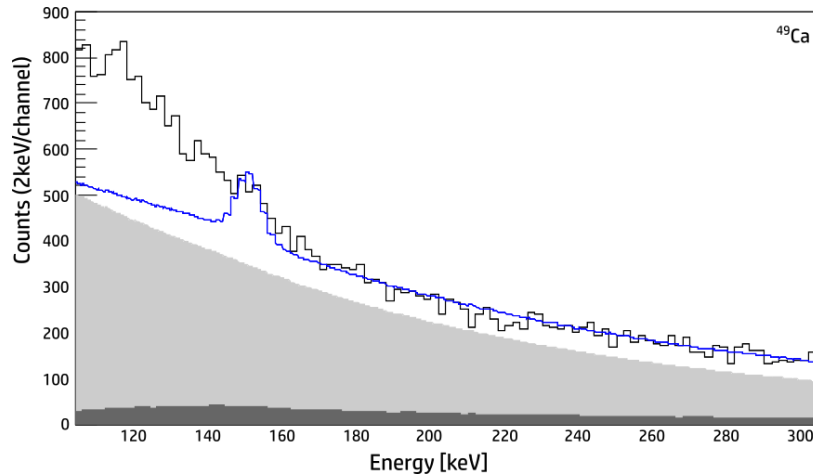
Figure 3.7: Gated and Doppler corrected γ-ray spectrum of ^{49}Ca, focusing on the 151keV γ-ray. The fitting algorithm does not have the capacity to fit the measured spectrum with reasonable certainty below 200keV, as shown. Due to the build-up of the background high energy X-rays in this region, the 151keV γ-ray is not resolved very well, introducing large uncertainty in the generated counts for this γ-ray.

identify the associated γ-ray energy. These simulations were folded into the fitting algorithm, fitting a large majority of the peaks found in the spectrum. This was actually the first test of the code as to whether it simply defines a peak based on the simulations, or was capable of discerning real peaks versus noise. Four simulated γ-rays in particular were fitted with parameters near zero, including multiple defined simulations per visually observed peaks. The results of the fits are shown in Table 3.2, along with the final fits for ^{48,49}Ca. The measured γ-ray spectrum, and the associated fit function, are shown in Figure 3.8.

3.3   Cross Sections

After generating the γ-ray yields and determining uncertainties in the measurements, the next step in analysis of the three nuclei was to generate cross sections from the yields. The relation for a γ-ray cross section is given by

$$\sigma_\gamma = \frac{N_\gamma}{(\rho t)N_i} \tag{3.4}$$

where ρt is the areal density of the target, N_γ is the counts of the particular γ-ray, and N_i is the total number of incoming ^{48,49}Ca particles [21]. N_γ is, of course, obtained from the fits, while N_i was generated by applying the PID gates to the S800 trigger. However, this value, even when modified due to the downscaling of the S800, doesn't accurately represent the number of incoming particles as portions of the particle beams were not detected by the S800 focal plane, ergo not included in the trigger. This was accounted for by factoring in the fraction of particles not detected by the S800. The acceptance ratio mentioned earlier was used as this factor, increasing the value of the gated S800 trigger, representing a more accurate number of incoming particles. With these counts available, the γ-ray cross sections were generated, and shown in Table 3.2.

By combining the γ-ray cross sections for each decay channel, as well as subtracting the cross sections from higher feeding states, the inelastic reaction population cross section σ_3 was calculated for each of the octupole vibration excitations for ^{48,49}Ca. For the 3_1^- state in ^{48}Ca, this population cross section was calculated to be 6.2(18)mb. In the case of ^{49}Ca, there were three states of interest, and their population cross sections are $\sigma(\frac{9}{2}_1^+) = 4.2(10)$mb, $\sigma(\frac{7}{2}_1^+) = 1.4(3)$mb, and $\sigma(\frac{5}{2}_1^+) = 1.4(3)$mb. All uncertainties were calculated in quadrature from the uncertainties in the γ-ray cross sections.
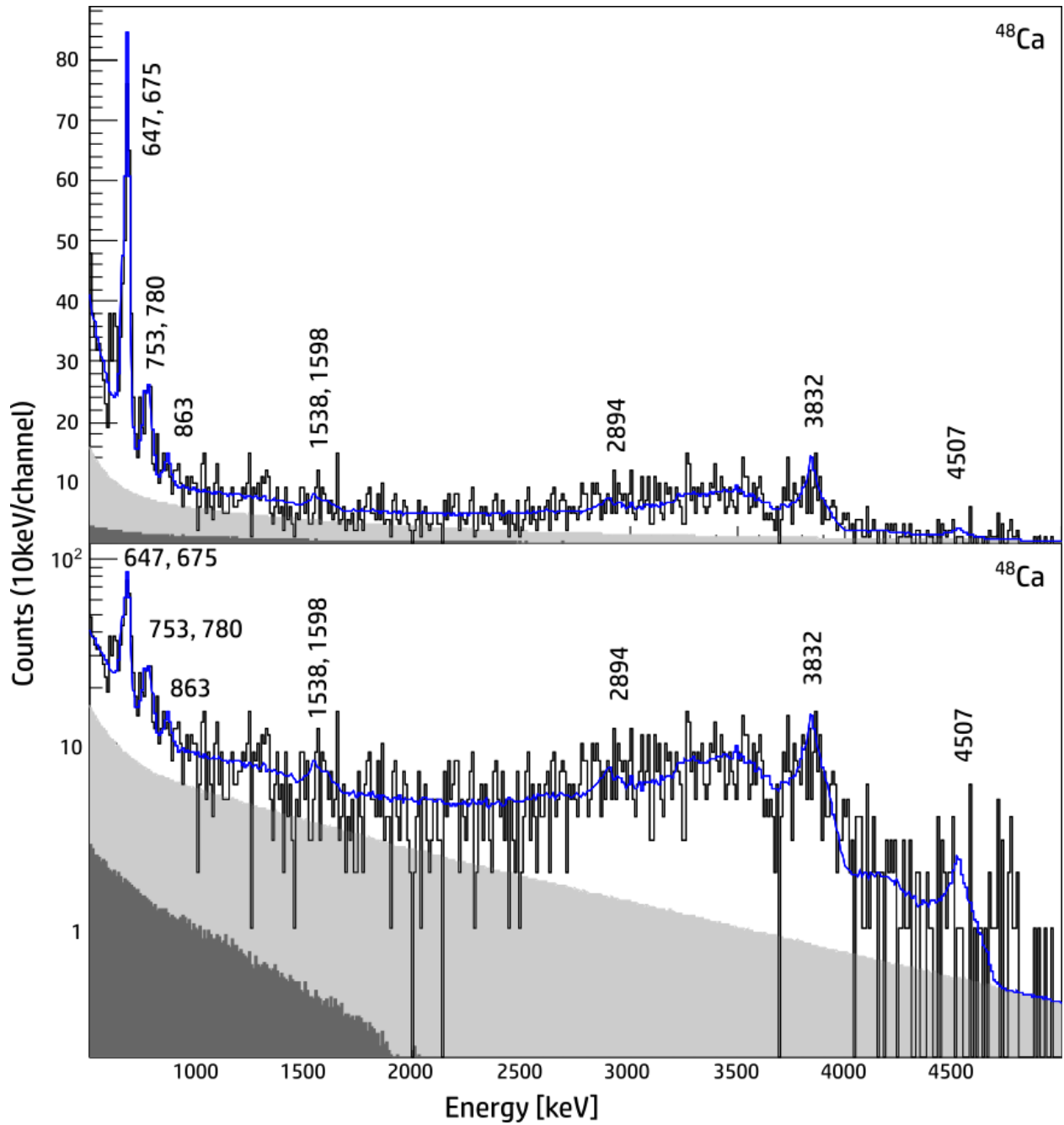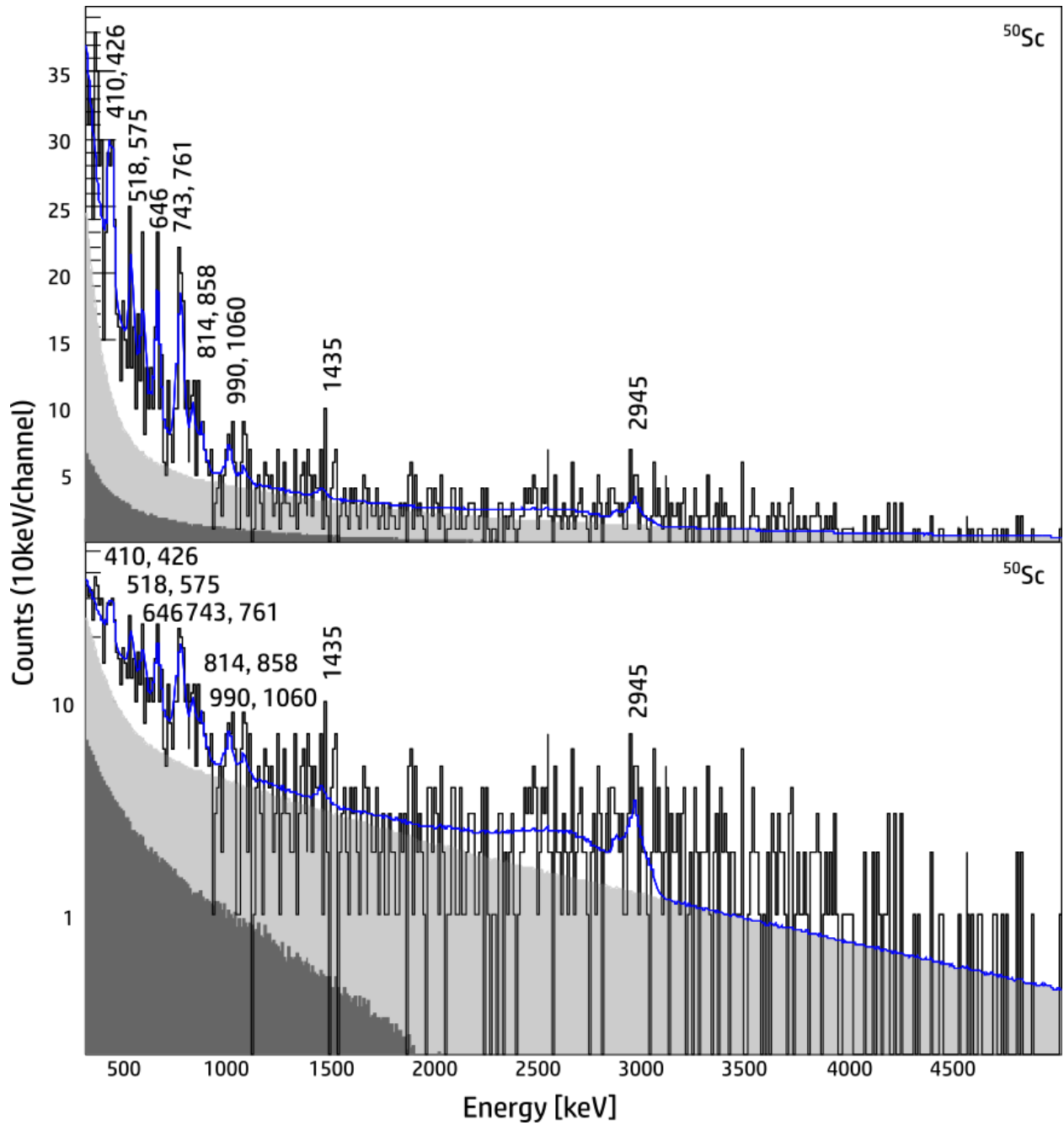
Figure 3.8: Gated and Doppler corrected γ-ray spectra for ^{50}Sc. The bottom spectrum is the logarithmic scale of the top spectrum. The measured spectra are shown in black while the fitted function defined by Equation 3.3 is shown as in blue. The background measurements are shown by the grey areas; prompt in light gray and non-prompt in dark gray.

3.4   Uncertainties and Errors

Accounting for uncertainty in the experiment, as well as statistical and systematic errors conducted in the experiment and analysis was taken into account in the data shown in Table 3.2. The starting place for uncertainty began with the statistical uncertainty of the fitting code. As ROOT fit each simulation peak to the measured, gated γ-ray spectrum, it generated an uncertainty value for each parameter fit in the code. This uncertainty was related to the proximity of the fit to the measured spectrum on a channel by channel basis. The closer the fit was to reproducing the measured spectrum, the lower the uncertainty was evaluated at. Again, this was done on a channel by channel analysis with each channel containing some component of each simulated spectrum as a fraction based on the parameter fit. Each parameter had its own associated uncertainty, and was used as the initial basis for accounting for total uncertainty in the measurements.

An additional source of uncertainty came from the accuracy of the GEANT simulation photopeak reproduction. Lew Riley concluded that the GEANT photopeak efficiency was within a 5% margin of error. Thus an added 5% uncertainty was added to the base uncertainty to account for this. Another source of uncertainty that was accounted for was the stopping power strengths of the GEANT code. These stopping powers modified how the approximation of the target thickness was deduced. If the stopping powers are too weak (strong), the effective target thickness is proportionally too high (low) [38]. Lew Riley investigated this issue and determined that the stopping powers introduced an additional 5% uncertainty to the measurements.

One more issue to address was an anomaly in the efficiency of GRETINA present in the data γ-ray spectra above 3MeV. During an unrelated experiment, focusing on pickup reactions to produce ^{49}Ca, users at the NSCL discovered that measurements of two particular γ-rays, 660keV and 3359keV (later corrected to 3356keV), were not in proportional amounts expected. The 660keV γ-ray cascades from high-lying state to a lower state that decays by a 3359keV γ-ray to the ground state. After the efficiency corrections were applied at the time, it was discovered that GRETINA was apparently detecting more of the 660keV γ-ray than the 3359keV. This does not make sense as cascade rules say that the 660keV γ-ray counts should be less than or equal to the 3359keV, not the other way around. However, it was discovered that the GEANT simulation analysis method actually accounts for this effect, and γ-ray yields generated by the fits show more counts in the 3356keV γ-ray than the 660keV as expected. Despite this, it was decided that an additional

uncertainty be added to the uncertainties already accounted for. As of the date of writing of this dissertation, the reason for this drop off in the raw GRETINA data was unknown as personnel at NSCL and BNL were investigating the issue. To deal with this unknown issue it was agreed that an additional 10% uncertainty would be added until this issue was further investigated.

Uncertainties shown in Table 3.2 are representative of the statistical uncertainties. They do not include the total systematic 20% uncertainty from the experiment and analysis method. However, the calculated cross sections from the above section do reflect the additional 20% systematic uncertainty.

Table 3.2: γ-ray yields from Doppler corrected and gated spectra for ^{48,49}Ca and ^{50}Sc. Intensity and cross section uncertainties are given in parenthesis for the last digit of value.

Nucleus	E_γ [keV]	E_i [keV]	$\rightarrow$	E_f [keV]	Intensity	Cross Section
^{48}Ca	648	5261		4613	10(4)	1.4(5)
	675	4507		3832	52(5)	7.3(7)
	754	5261		4507	9(4)	1.3(5)
	780	4613		3833	13(4)	1.9(5)
	863	5370		4507	5(3)	0.7(4)
	1538	5370		3832	4(3)	0.6(5)
	1598	6105		4507	3(3)	0.4(5)
	2894	7401		4507	12(4)	1.7(6)
	3832	3832		0	100(5)	14.2(7)
	4507	4507		0	20(3)	2.8(5)
^{49}Ca	151	4016		3865	29(4)	1.5(2)
	547	5683		5136	1(2)	0.1(1)
	660	4016		3356	75(3)	3.7(2)
	743	4759		4016	28(2)	1.4(1)
	875	4891		4016	7(2)	0.4(1)
	923	5682		4759	9(2)	0.4(1)
	1120	5136		4016	8(2)	0.4(1)
	1431	4787		3356	8(2)	0.4(1)
	1667	5683		4016	3(2)	0.2(1)
	2023	2023		0	10(3)	0.5(1)
	3356	3356		0	100(5)	5.0(2)
	3585	3585		0	29(3)	1.4(3)
	3867	3867		0	38(5)	1.9(3)
	4016	4016		0	28(4)	1.4(2)
	4469	4469		0	28(2)	1.4(1)
^{50}Sc	410				32(22)	1.1(7)
	426				40(22)	1.3(7)
	518				45(20)	1.5(7)
	575				35(19)	1.2(6)
	646				73(21)	2.4(7)
	743				53(30)	1.8(10)
	761				90(32)	3.0(11)
	814				44(20)	1.5(7)
	858				38(20)	1.3(6)
	990				38(19)	1.2(6)
	1060				22(18)	0.7(6)
	1435				18(20)	0.6(7)
	1504				3(24)	0.1(8)
	2853				22(30)	0.7(10)
	2945				100(34)	3.3(11)

CHAPTER 4

DERIVED ANALYSIS

4.1   Level Schemes

Comparing the γ-ray yields from each nucleus with the currently known data on each, as well as with the available $\gamma\gamma$ coincidence spectra from e11037, level schemes were generated for ^{48,49}Ca. Unfortunately, despite getting fairly clean readings on the low-energy γ-rays present in the gated spectra, it was not possible to generate a level scheme for ^{50}Sc due to lack of information, particularly lack of $\gamma\gamma$ coincidence counts as well as generally low statistics in the γ yields in general. The level schemes for ^{48,49}Ca are shown in Figure 4.1.

The level schemes, especially the spin and parity assignments, were built by comparison of the γ-ray yields with literature available on the calcium isotopes. Montanari, *et al.*, performed state lifetime measurements using heavy ion transfer reactions of ^{48}Ca on ^{64}Ni and ^{208}Pb targets [39]. Kashy, *et al.*, measured the angular distributions to define spin and parity assignments for ^{49}Ca using ^{48}Ca(d,p)^{49}Ca reactions and distorted wave Born approximation (DWBA) calculations [40]. Broda published several papers outlining their work analyzing data taken from heavy ion transfer reactions involving ^{48}Ca, similar to those of Montanari, using ^{48}Ca, ^{208}Pb, and ^{238}U [41] [42]. Feldman, *et al.*, used 200MeV and 318MeV protons to measure neutron transition densities of low-lying states in ^{48}Ca, with additional extended random phase approximation (ERPA) calculations as comparison [1]. Additional sources used in the determination of the spin and parity assignments included works by Fujita [^{48}Ca(p,p$'$)], Vanhoy [^{48}Ca(n,n$'\gamma$)], Wise [^{48}Ca(e,e$'$)], and Canada [^{48}Ca(d,pγ)^{49}Ca] [43] [44] [45] [46].

Please note that spin and parity assignments that were not fully established are placed in parentheses, and the subscript i of the assignment is given as the ith state of that spin-parity in the level scheme above the ground state. Most energies stated have an uncertainty of 2-4keV, assigned due to the resolution capabilities of the GRETINA-S800 detector system as well as the quality of previous measurements of ^{48,49}Ca and ^{50}Sc. The energies stated correspond to values in correlation with γ-ray peaks found in the Doppler corrected γ-ray spectrum for each nucleus.
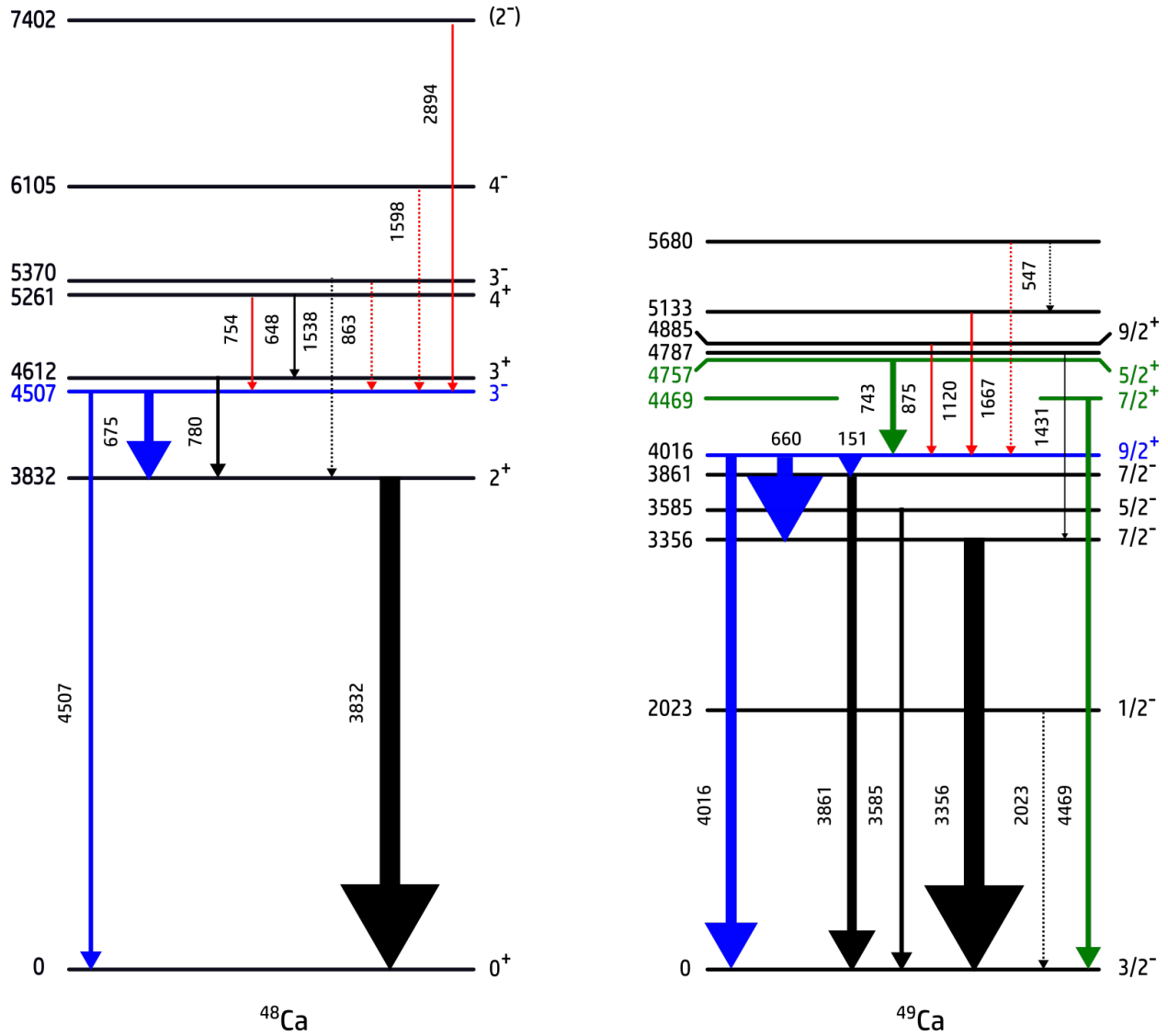
Figure 4.1: Energy level schemes for ^{48}Ca and ^{49}Ca as constructed from γ-ray yields, known spin-parity assignments, energy levels. All energies in keV. Thickness of arrows indicates intensity of each γ-ray decay, as shown in Table 3.2. Blue lines and arrows indicate the octupole states of primary interest, red arrows indicate feeding states to these primary octupole states, and green lines and arrows indicate additional octupole states in ^{49}Ca.

4.1.1 ^{48}Ca

The ground state of ^{48}Ca, as a nucleus with even numbers of both protons and neutrons, has a spin-parity assignment of 0^+ along with a spherical shape given its double closed shell nature. The first excited state sits at an energy of 3832keV above the ground state, and assigned with a spin-parity of 2^+. This energy level has a single γ-ray decay channel of energy equal to its state energy. Montanari measured the reduced transition rate from this state to the ground state through lifetime measurements, generating a value of $B(E2; 2_1^+ \rightarrow 0^+) = 1.9(2)$ Weisskopf units [W.u.] [39]. The decay γ-ray from this state was the largest contributor to the gated γ-ray spectrum for ^{48}Ca, and all intensities listed for γ-rays for this nucleus in Table 3.2 are given as percentages of this γ-ray.

The next excited states are two very closely spaced states, separated by about 4keV. Experiments performed by Feldman, Wise, and others were not generally able to resolve this doublet, however neutron scattering measurements by Vanhoy were able to do so and properly assign spin-parity assignments to the two states. The lower state, at 4503keV, had been previously suggested in β-decay measurements, and through evaluation of the Legendre coefficients for the 671keV γ-ray decaying to the 2_1^+ state Vanhoy defined the spin-parity assignment for this state as 4_1^+. The state just above it, at 4507keV, had been given the assignment 3_1^- by Vanhoy using the same method as teh 4_1^+ state, as well as being defined as such by Feldman, Wise, and others.

The close proximity of these two states initially presented an issue in analyzing the lowest-lying octupole vibration excitation, the 3_1^- state, in this nucleus. This was due, in part, to the low statistics of the ^{48}Ca data. Present in the γ-ray spectrum for this nucleus were three doublets, 671/675keV, 754/758keV, and 863/867keV, that were not fully resolved that are associated with the close spacing of these two states. However, it was determined that the 4_1^+ state was not strongly populated during e11037, particularly due to the lack of presence of γ-rays specifically associated with the 4_1^+ state and not the 3_1^- state. Two such γ-rays, 469keV and 1226keV, were not detected in significant amounts in the γ-ray spectrum for ^{48}Ca, leading to the idea that the 4_1^+ state was not significantly populated due to proton scattering. This idea was substantiated by remarks by Feldman. As mentioned earlier, Feldman published measurements on the neutron transition densities for the 3_1^- state and their ERPA calculations were in excellent agreement with

their findings. They also folded ERPA calculations for the 4_1^+ state into the 3_1^- data, resulting in negligible differences between the original 3_1^- calculations and 4_1^+ folded neutron densities.

While the data was not able to physically resolve the doublet issue, statistically there were reasons to agree with the argument by Feldman, *et al.* All decay channels of the $4_1^+ - 3_1^-$ doublet were simulated and folded into the fitting code, as well as run through the stability test mentioned earlier. In the early stages of fitting, when the simulation parameters had not been well established, the γ-rays associated with the 4_1^+ state were fitted with non-zero values, particularly at the extreme resolutions. However, these values were smaller than the statistical uncertainties generated in the fit, as well as being significantly smaller than counts in the γ-rays associated with the 3_1^- state. After the simulation parameters had been well defined, in almost every case the fitting code generated zero value parameters for the 4_1^+ γ-rays, and in cases of non-zero values the statistical uncertainties were, again, larger than the values fitted. This, along with the negligible counts in the 469keV and 1226keV γ-rays associated with states that do not decay to the 3_1^- state, gives weight to the argument that the 4_1^+ state was not significantly populated due to inverse kinematic proton scattering. For this reason, the 4_1^+ state was not drawn in Figure 4.1.

The 3_1^- state has two γ-decay channels, an octupole E3 transition to the ground state with a γ-ray energy of 4507keV and a mixed dipole E1/quadrupole M2 transition to the 2_1^+ state as a 675keV γ-ray. Montanari generated a reduced transition rate for the transition to ground state of $B(E3; 3_1^- \rightarrow 0^+) = 6.8(10)$W.u [39]. This 675keV γ-ray was the strongest of the two decay channels for this state. This state, given its spin-parity assignment in comparison to the ground state, as well as strong $B(E3)$ value, is defined as the lowest-lying octupole state in ^{48}Ca.

The state just above the 3_1^- and 4_1^+ rests at an energy of 4612keV above the ground state, and has been given the spin-parity assignment of 3_1^+ by Feldman and Wise. It has only one decay channel, a 780keV γ-ray leading to the 2_1^+ state.

The next state identified as being populated during e11037 sits at an energy of 5260keV above the ground state. This state has been shown to have three decay channels, a 648keV γ-ray to the 3_1^+ state, and a doublet containing 754keV and 758keV γ-rays to the 3_1^- and 4_1^+ states respectively. As mentioned earlier, it was believed that the 4_1^+ state was not significantly populated, therefore the statistical counts generated by the fitting code for this doublet were assigned to the 754keV γ-ray. The spin-assignment for this state is not conclusive as few of the sources mentioned earlier

specifically define the assignment. Some of the sources show assignments of (5^+), while others list either (4^+) or (4^-). Only Vanhoy specifically defined the state as 4_2^+, which was used in the level scheme.

Another state involved in the 3_1^- vs. 4_1^+ issue is the 3_2^- state sitting at 5370keV above the ground state. This state also has three decay channels, a 1538keV γ-ray to the 2_1^+ state and the 863/867keV doublet to the 3_1^- and 4_1^+ states. Pointing to the arguments made above, the major contribution to the doublet was assigned to the 863keV γ-ray in association with the 3_1^- state.

The final two states identified by γ-ray decays in the ^{48}Ca γ-ray spectra sit at energies of 6105keV and 7402keV above the ground state. Unlike other states well above the $3_1^-/4_1^+$ doublet, these two states do not have associated decays to both members of the doublet. In fact, both only have decays to the 3_1^-. While there are other decay channels available for both states, only the 1598keV γ-ray for the 6105keV and 2894keV γ-ray from the 7402keV state were detected in significant amounts. Wise, Feldman, and Vanhoy assigned the spin-parity 4_1^- to the 6105keV state. The 7402keV state, however, is poorly defined in spin-parity, like the 5260keV state. Two different assignments were found in the sources mentioned, (4^-) and (2^-), with little evidence to support either. Thus the assignment placed in the level scheme was the same (2^-) assignment made in the Evaluated Nuclear Structure Data Files [47].

4.1.2 ^{49}Ca

The ground state in ^{49}Ca has been shown by angular distribution measurements of cross sections from $^{48}Ca(d,p)^{49}Ca$ experiments by Kashy to have a spin assignment of $\frac{3}{2}$. This is consistent with their own shell model calculations, based on the configuration of the valence neutron occupying the $1p_{\frac{3}{2}}$ shell. The first excited state sits at an energy of 2023keV, and was given a spin-parity assignment of $\frac{1}{2}_1$ by Kashy. This was based on the single neutron transition from the $1p_{\frac{3}{2}}$ shell to the $1p_{\frac{1}{2}}$ shell. As the first excited state, the only available decay channel available is a single γ-decay of equl energy to its state energy.

The next excited state identified by association of the γ-ray spectrum for ^{49}Ca is the 3356keV state. There is very little definitive information on this state. The spin-parity assignment has been proposed as various values. Kashy associated the state with the $1d_{\frac{5}{2}}$ shell occupation and an assignment of $(\frac{5}{2})$ [40]. Canada gave an assignment of $(\frac{9}{2}^+)$, as did Broda initially, though in a later paper Broda gave an assignment of $(\frac{7}{2}^-)$. This later assignment coincides with the

ERPA calculations of Montanari, thus this level was given the assignment of $\frac{7}{2}^-_1$ for the purpose of this dissertation. Given this assignment, this state has the characteristics of the lowest-lying quadrupole vibration excitation. Montanari also measured the lifetime of this state as 3.5(12)ps and therefore determined the reduced transition strength from this state to the ground state as $B(E2; \frac{7}{2}^-_1 \rightarrow \frac{3}{2}^-) = 0.05(2)$W.u. based on their lifetime measurements of this state. This state has a single γ-decay of energy equal to its state energy, and is the largest contributor to the ^{49}Ca γ-ray spectrum, but not by a large margin in comparison to the corresponding state in ^{48}Ca. All intensities for ^{49}Ca in Table 3.2 are percentages of the γ-ray counts decaying from this $\frac{7}{2}^-_1$ state.

Above the 3356keV state sits a 3585keV state with a spin-parity assignment of $\frac{5}{2}^-_1$. It has a single decay channel of energy equal to its state energy directly to the ground state. This spin-parity assignment is consistent with the $^{48}Ca(d,p)^{49}Ca$ measurements performed by Kashy and ERPA calculations by Montanari [40] [39].

The next state identified by γ-rays found in the spectrum of ^{49}Ca sits at an energy of 3867keV. Like the other excited states below it, it has a single decay channel associated with it as a transition directly to the ground state. Curiously, this particular state was not reported by Montanari nor by Kashy. When comparing the placement of this energy level to states calculated by shell model calculations performed by Volya and Kravvaris, this state corresponds to a $\frac{7}{2}^-_2$ state of similar energy. No other information was available to counter this definition, thus the assignment made for this state is the shell model assignment.

Not drawn in the level scheme for ^{49}Ca, Figure 4.1, is a state that sits at an energy around 3991keV, about 25keV below the 4016keV state. In early papers published on this nucleus, these two states were not easily resolved, but some experiments were able to resolve this doublet, such as work done by Kashy. In fact, due to the lack of high energy resolution, this doublet barely appears in the gated ^{49}Ca γ-ray spectrum. Montanari placed this energy level in their level scheme with a spin-parity assignment of $\frac{5}{2}^-_2$, which is supported by most sources cited, including $^{48}Ca(d,p)^{49}Ca$ measurements. Despite this assignment, it was not placed in the level scheme as no specific γ-ray counts for its single decay channel were generated.

As mentioned above, the 3991keV in early experiments was easily confused with the 4016keV state fully resolved in later experiments. Once fully resolved, the spin-parity assignment was rather clear for this state. Kashy determined that this state was created by the promotion of the $1p_{\frac{3}{2}}$

ground state neutron to the $1g_{\frac{9}{2}}$ intruder shell. Further experiments also gave this state a positive parity, yielding a full assignment of $\frac{9}{2}^+_1$. This parity and spin promotion in comparison to the ground state is a signature of the first octupole vibrational state in ^{49}Ca. The state decays by three γ-rays, a primary 660keV γ-ray to the 3356keV $\frac{7}{2}^-_1$ state, and two weak decays of 4016keV directly to the ground state and 151keV to the 3867 $\frac{7}{2}^-_2$ state. Montanari measured the lifetime of this state to be 8.5(20)ps, and determined the reduced transition rate for this state decaying to the ground state as $B(E3; \frac{9}{2}^+_1 \rightarrow \frac{3}{2}^-) = 7.9(20)$W.u.

The next energy level in the scheme is a previously undiscovered state that sits at an energy about 4469keV. An anomalous peak in the ^{49}Ca γ-ray spectrum at that energy was discovered. GEANT simulations were performed for this γ-ray peak, and statistically significant counts were generated. This specific γ-ray doesn't fit as a deexcitation from any of the known energy levels for ^{49}Ca. It also does not present any $\gamma\gamma$ coincidence spectra with any of the other known γ-rays for this nucleus. It did not appear to be a contaminant γ-ray from nuclei in proximity to ^{49}Ca in the PID spectra.

As stated above, one member of the octupole vibration multiplet had already been well established for ^{49}Ca, however, there were other possible multiplet members evident in the data from e11037. The 3^-_1 state in ^{48}Ca can couple with the valence $p_{\frac{3}{2}}$ neutron to produce a quadruplet of states, $\frac{9}{2}^+, \frac{7}{2}^+, \frac{5}{2}^+, \frac{3}{2}^+$. Given the strength of the population of the 4469keV state in the present data, it is possible that this state is a member of the multiplet. The next known energy level sits at an energy of 4759keV. It has only one decay channel; a 743keV γ-ray to the $\frac{9}{2}^+_1$ state. Once again, due to the strength of the population of this state implies that it is a member of the octupole multiplet. The assignments of the spin-parity of $\frac{5}{2}^+_1$ to the 4759keV state and $\frac{7}{2}^+_1$ to the 4469keV state shown in Figure 4.1 are not definitive and are simply proposed given the arrangement of the states.

Beyond this lay four higher energy states based on γ-rays found in the gated ^{49}Ca γ spectrum. A weakly populated state at 4787keV state is seen in the γ-ray spectrum, with a single decay channel of a 1431keV γ-ray to the $\frac{7}{2}^-_1$ state. No spin-parity assignment is known for this state, and given the weakness of this state's population it is unlikely to be a member of the octupole multiplet. The 4885keV state above the ground state presented in the level scheme has a single decay channel; 875keV to the $\frac{9}{2}^+_1$ state. The literature gives this state a spin-parity assignment $\frac{9}{2}^+_2$. The final two

states have no known assignments. The 5133keV state has only one decay channel as a 1120keV γ-ray to the 4017keV $\frac{9}{2}_1^+$ state. The 5680keV state has three decay channels; a 547keV γ-ray to the 5133keV state, a 923keV decay to the 4759keV state, and a 1667keV γ-ray to the 4016keV $\frac{9}{2}_1^+$ state.

4.1.3 ^{50}Sc γ-rays

As mentioned in the previous chapter, very little information is available on the ^{50}Sc isotope. Furthermore, what little information is available does not reflect reactions capable of producing negative parity states in comparison to the known 5^+ ground state. Worse, the isotope has an isomeric state resting at 257keV with a mean lifetime of 0.35s, which translates into an unknown ratio of ground state to isomeric state ^{50}Sc particles reacting with the liquid hydrogen target. Worst of all, the statistical data found in the e11037 data contains very low rates for this nucleus. Approximately 1.6×10^6 ^{50}Sc particles were produced, in comparison to 4.7×10^6 ^{48}Ca and 3.8×10^7 ^{49}Ca particles generated during e11037.

A total of 15 γ-rays were detected for this nucleus, and there does not appear to be contamination from surrounding nuclei in the PID gates. The γ-rays and their intensities are shown in Table 3.2. Without establishment of the level scheme, it was not possible to continue analysis of the ^{50}Sc. New γ-rays were discovered for this nucleus, but that was about it. In addition to this, information necessary to continue the analysis, such as reduced transition rates, was not available to allow further derivation of information possible in ^{48,49}Ca.

4.2 FRESCO

The next phase of analysis of the low-lying octupole vibrations in ^{48,49}Ca focused on extracting the proton scattering deformation length $\delta^{(p,p')} = \delta_3$, which is the amplitude of the total octupole vibration. This was accomplished through the use of coupled channels calculations using the analysis code FRESCO [48]. These calculations generated various reaction cross sections, including the inelastic reaction cross section populating the octupole vibration excitations from the ground state. By matching these inelastic reaction cross sections to the measured population cross sections from the e11037 data, the deformation length for the octupole vibrational states in ^{48,49}Ca was generated.

The FRESCO analysis code was chosen for the coupled channels calculations as it is capable of handling relativistic calculations as well as the appropriate spin assignments and full potential

descriptions of ^{48,49}Ca nuclei. The calculation input files were built step by step with the assistance of Dr. Kirby Kemper to first reproduce, within reason, the coupled channels calculations performed by Dr. Lew Riley for his analysis of the ^{48,50}Ca nuclei. Riley used the analysis code ECIS for his calculations, and it was initially decided that the analysis for ^{48,49}Ca for the present dissertation would be conducted with the same code. However, ECIS was unable to accept the exact spin assignments for the states in ^{49}Ca.

With Dr. Kemper's assistance, FRESCO input files were built to generate calculation outputs for ^{48}Ca that closely matched the output of the ECIS code. In particular, the angular distributions of the differential inelastic cross sections for ^{48}Ca were used as a point of comparison. An example of these distributions is shown in Figure 4.2. By closely matching these distributions between FRESCO and ECIS, the basic calculation templates were established. Minor differences in the distributions were observed which were the result of minor differences in the operation of the two codes. For example, the center-of-mass energies in FRESCO were 0.4MeV higher than in ECIS. In addition, ECIS takes as an input the deformation parameter, β_3, where FRESCO uses the deformation length $\delta_3 = R_0\beta_3$ as an input. This does produce subtle differences in how the two codes deform the optical potentials to simulate the octupole vibrations, but this effect was accounted for by matching the β_3 in each code. After all inputs in the FRESCO code were optimized to reproduce the ECIS calculations for ^{48}Ca, similar input files were generated for ^{49}Ca. The parameters for the optical potentials used in the FRESCO calculations were determined using fitted equations published by Koning and Delaroche [49] and are shown in Table 4.1.

4.2.1 3_1^- in ^{48}Ca

To analyze the lowest-lying octupole state in ^{48}Ca, the parameters for the FRESCO calculations were defined to generate reaction cross sections, including the Doppler corrected energy of the protons in the inverse kinematic scattering field. The relativistic calculations were done by hand and generated the energy of the proton nuclei in the ^{48}Ca ion reference frame to be $E_p = 98.89$MeV. Using this, along with the nucleon numbers of ^{48}Ca, the global optical parameters were generated, and are shown in Table 4.1. These values were written into the FRESCO input file, along with the octupole deformation length, δ_3. This value was scanned across a range of values to generate the inelastic reaction cross section for populating the 3_1^- state from the 0^+ ground state. By scanning across multiple values of δ_3, the calculated cross section was matched to the measured
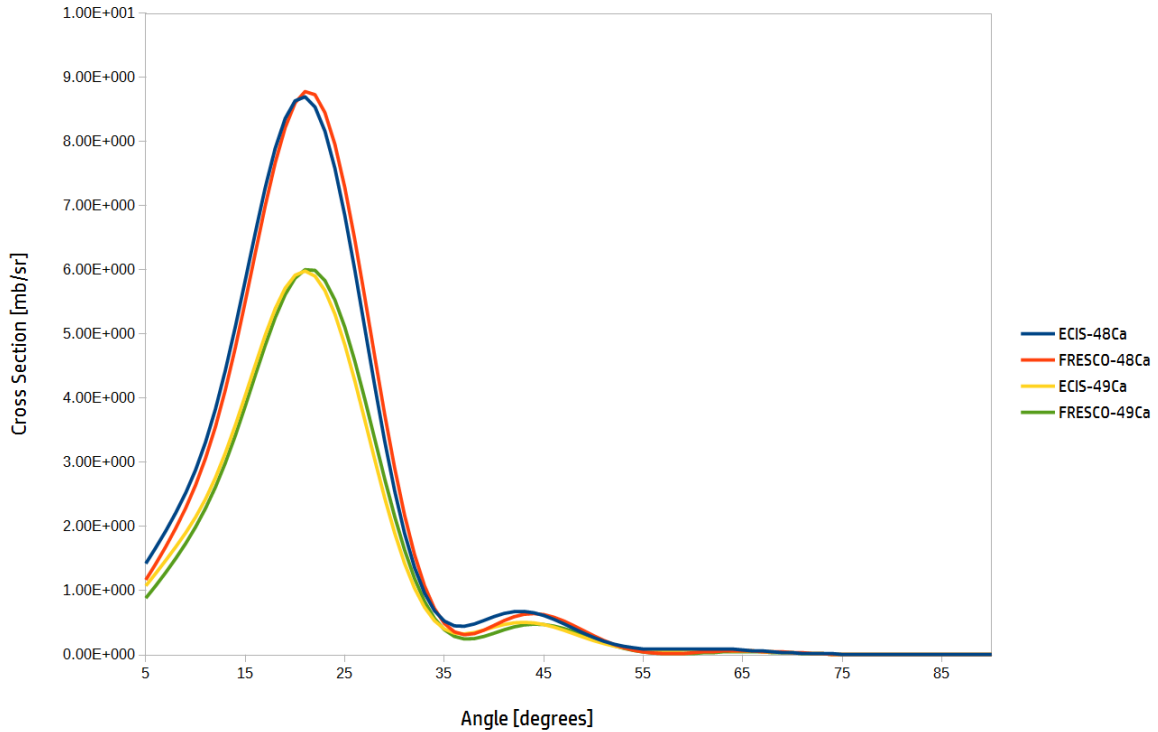
Figure 4.2: Comparison of coupled channels calculations by the analysis codes ECIS and FRESCO for ^{48,49}Ca. The FRESCO input files were fine tuned using ECIS calculations already performed on ^{48}Ca, and once confirmed the output from ECIS calculations for ^{49}Ca were able to closely match new FRESCO calculations for that nucleus.

Table 4.1: Global optical parameters derived from relations published by Koning and Delaroche. Parameters used in potential forms of the standard nuclear Woods-Saxon potential.

Nucleus	V_V	W_V	R_V	a_V	W_S	R_S	a_S	V_{SO}	W_{SO}	R_{SO}	a_{SO}
^{48}Ca	27.550	9.912	1.192	0.671	1.805	1.285	0.544	3.960	-0.953	1.007	0.590
^{49}Ca	28.690	9.638	1.193	0.671	2.001	1.284	0.544	4.027	-0.902	1.009	0.590

reaction cross section from the previous chapter. The value of the δ_3 parameter set in the macro file that ultimately matched the two cross sections represented the amount by which the nucleus was deformed on average during the lowest-lying octupole vibration excitation. The resulting value for the 3_1^- state in ^{48}Ca was $\delta_3 = 1.0(2)fm$.

4.2.2 $\frac{9}{2}_1^+$, $\frac{7}{2}_1^+$ $\frac{5}{2}_1^+$ in ^{49}Ca

The analysis of the octupole states in ^{49}Ca was performed in a similar manner. The proton energy used in the FRESCO input files for this nucleus was calculated by hand to be $E_p = 94.78$MeV. This energy was programmed into the input files along with the optical parameters for this nucleus, shown in Table 4.1. Using the same scanning technique to match the calculated cross sections to the measured cross sections, the deformation lengths for the three known octupole vibration states in ^{49}Ca were extracted from the FRESCO calculations. The values extracted were $\delta_3 \left(\frac{9}{2}_1^+ \right) = 1.2(1)$fm, $\delta_3 \left(\frac{7}{2}_1^+ \right) = 1.5(2)$fm, and $\delta_3 \left(\frac{5}{2}_1^+ \right) = 1.1(1)$fm.

A note on error propagation. The value of the measured cross sections shown in the previous chapter are, again, $\sigma \left(3_1^-, ^{48}Ca \right) = 6.2(18)$mb, $\sigma \left(\frac{9}{2}_1^+, ^{49}Ca \right) = 4.2(10)$mb, $\sigma \left(\frac{7}{2}_1^+, ^{49}Ca \right) = 1.4(3)$mb, and $\sigma \left(\frac{5}{2}_1^+, ^{49}Ca \right) = 1.4(3)$mb. The original uncertainty in the measured cross sections for the 3_1^- state in ^{48}Ca was about 29% of the value given, and the uncertainty shown for the $\frac{9}{2}_1^+$ state in ^{49}Ca was about 24% of the value shown. The uncertainty for the other two states is about 21%. These relative uncertainties include not only the statistical uncertainty, but the additional 20% systematic uncertainty defined in the previous chapter.

The cross sections calculated by the FRESCO code are proportional to the square of the deformation lengths entered as input in the calculations, therefore the extraction of the deformation lengths is proportional as a square root to the original cross section. Therefore, as a consequence of the propagation of error, the relative uncertainty in the deformation length should be one half of the relative uncertainty of the cross sections. The uncertainties shown for these deformation lengths reflect this difference in relative uncertainties. About 14.5% for the 3_1^- state in ^{48}Ca, 12% for the $\frac{9}{2}_1^+$ state in ^{49}Ca, and 10.5% in the remaining two octupole states.

4.3 Nuclear Fluid Deformation Lengths

With the proton scattering deformation lengths in hand, the final phase of computational analysis was to use Equation 1.3 to extract the proton and neutron octupole deformation lengths. As mentioned earlier, this is accomplished using two experimental probes. In addition to the inverse kinematic proton scattering experiment, lifetime measurements performed by Montanari were used in this analysis. The lifetime measurements were converted into reduced transition rates for the states of interest, and mentioned above in the explanation of various states in ^{48,49}Ca. These transition rates are directly relatedd to the proton deformation length by the equation [50]

$$\delta_p = \frac{R_0}{Z(\lambda+3)}\sqrt{4\pi B(E\lambda)(2\lambda+1)} \tag{4.1}$$

where $R_0 = 1.2A^{\frac{1}{3}}$fm, Z is the charge of the nucleus, λ is the multipolarity of the vibration, and $B(E\lambda)$ is the reduced transition rate. As mentioned earlier, the reduced transition rates for deexciting the octupole ($\lambda = 3$) vibrational states measured through lifetime measurements performed by Montanari, *et al*, are $B\left(E3,^{48}Ca; 3_1^- \to 0^+\right) = 6.8(10)$W.u. and $B\left(E3,^{49}Ca; \frac{9}{2}_1^+ \to \frac{3}{2}^-\right) = 7.9(20)$W.u. The proton deformation lengths for the octupole vibrational states were calculated using these reduced transition rates and Equation 4.1 to be $\delta_p\left(3_1^-\right) = 0.9(1)$fm and $\delta_p\left(\frac{9}{2}_1^+\right) = 1.0(1)$fm. The uncertainties in these proton deformation lengths do reflect one half of the relative uncertainty of the reduced transition rates. Unfortunately, transition rates for the $\frac{7}{2}_1^+$ and $\frac{5}{2}_1^+$ states were not available, therefore a proton deformation length could not be calculated for these states.

With the definition of the proton deformation lengths, the calculation of the neutron deformation lengths for the 3_1^- and $\frac{9}{2}_1^+$ states was a simple process using Equation 1.3. As mentioned previously, the low energy, $E_p \sim 10$MeV, interaction strength of the proton scattering probe with the neutron component of the target nucleus is three times stronger than the strength with the protons, but for high energy protons, $E_p > 1$GeV, the proton and neutron components are nearly indistinguishable. This yields two values for the ratio of the neutron to proton interaction strengths for proton scattering, $b_n/b_p = 1, 3$ [12]. For e11037, the average energy of the protons with respect to the beam projectile frame was ~ 95MeV, placing this experiment in between the two energy ranges. To account for this, both values of the ratio were used in calculating the neutron deformation lengths. This established the minimum and maximum values the deformation lengths could reach. The values of the lengths were defined as the average across these ranges, and the uncertainties

were defined as the difference between the means and the extrema. These calculations were also performed using the maxima and minima of the proton deformation lengths as well as the total deformation lengths, δ_3. This yielded the values of the neutron deformation lengths of the lowest-lying octupole vibrations as $\delta_n\left(3_1^-\right) = 1.1(3)$fm and $\delta_n\left(\frac{9}{2}_1^+\right) = 1.3(3)$fm.

The components of the uncertainties in these neutron deformation lengths include the statistical and systematic uncertainties described in Section 3.4, the uncertainty in the reduced transition rates published by Montanari, *et al*, as well as the relative uncertainty in the interaction strength of the proton probe with the two components of the nucleus. As mentioned above, the values and uncertainties were established using the minima and maxima of values generated across values of δ_3, δ_p, and the interaction strength ratio b_n/b_p. By comparing the average standard of deviation across the values of δ_n for each range, the component of each range contributing to the uncertainties in the neutron deformation lengths was determined. The statistical and systematic uncertainty in the total nuclear deformation length, δ_3, contributes the bulk of the total standard deviation as roughly 67% of the uncertainties. The uncertainty in the interaction strength ratio, given the average beam energy of the proton scattering probe, contributes approximately 23% of the uncertainties. Lastly, the uncertainties of the Montanari lifetime measurements, translated into the reduced transition rates and proton deformation lengths, contributes around 10% of the uncertainties in the neutron deformation lengths.

4.4   Discussions

Equation 1.2 shows that the neutron to proton transition matrix element ratio M_n/M_p is equal to the ratio of the neutron number times the neutron deformation length $(N\delta_n)$ to the proton number times the proton deformation length $(Z\delta_p)$. In the homogeneous collective models Bernstein, Brown, and Madsen describe, the protons and neutrons vibrate with the same amplitude, yielding the M_n/M_p ratio equal to N/Z. They compiled information on various hadron scattering experiments, including a range of calcium, nickle, and tin isotopes, that shows that nuclei don't necessarily follow the homogeneous collective model. By comparing Equations 1.2 and 1.3, the deformation lengths of two probes, F and G, can be related by the relation [11]

$$\frac{M_n}{M_p} = \frac{\epsilon_G^F \frac{\delta^F}{\delta^G} - 1}{\frac{b_n^F}{b_p^F} - \frac{b_n^G}{b_p^G}\epsilon_G^F \frac{\delta^F}{\delta^G}} \tag{4.2}$$

where

$$\epsilon_G^F = \frac{1 + \frac{N}{Z}\frac{b_n^F}{b_p^F}}{1 + \frac{N}{Z}\frac{b_n^G}{b_p^G}} \tag{4.3}$$

and $b_{n(p)}^{G,F}$ are the interaction strengths of the probes F and G with the neutron (proton) mean field component of the nucleus. By using the lifetime measurements used earlier, the interaction strengths for one of the probes simplifies to 0 for neutrons and 1 for protons, simplifying the relation for M_n/M_p to [51]

$$\frac{M_n}{M_p} = \frac{b_p^{(p,p')}}{b_n^{(p,p')}} \left[\frac{\delta^{(p,p')}}{\delta_p} \left(1 + \frac{b_n^{(p,p')}}{b_p^{(p,p')}} \frac{N}{Z} \right) - 1 \right] \tag{4.4}$$

where $\delta^{(p,p')} = \delta_3$. Using the same values of the interaction strength ratios, 1 and 3, along with the maxima and minima of δ_3 and δ_p, the upper and lower limits of the M_n/M_p values were established in the same manner as the neutron deformation lengths. The average over these ranges was used to define the values of the M_n/M_p ratios, and the uncertainties were defined as the difference between these averages and the limits, yielding the values $M_n/M_p\left({}^{48}Ca, 3_1^-\right) = 1.7(6)$fm and $M_n/M_p\left({}^{49}Ca, \frac{9}{2}^+_1\right) = 2.0(0)$fm. A comparison of the previously known M_n/M_p ratio for ^{48}Ca with the values generated from the data from e11037 is shown in Table 4.2, and a visual representation of these values, including the values generated for ^{49}Ca is shown in Figure 4.3. The calculation of the M_n/M_p ratios was identical in form to the neutron deformation lengths. Thus the contribution of the statistical and systematic uncertainties in the measured cross sections to the uncertainties of the M_n/M_p values is about 67%. The uncertainty in the interaction strength ratio is roughly 23%, and the Montanari uncertainties contribute approximately 10% of the total uncertainties of the M_n/M_p values.

In the effort to understand these derived values, shell model calculations for ^{48,49}Ca and ^{50}Sc were performed by Dr. Alexander Volya and Konstantinos Kravvaris. Using a various interaction models, Volya and Kravvaris were able to generate reasonably accurate estimates of the energy levels and transition strengths in ^{48}Ca, as well as the negative parity states in ^{49}Ca. However, due to the limitations of the shell model approaches, including the fact that currently available interaction models do not include the $1p_{\frac{9}{2}}$ shell, the shell model calculations were not able to improve the understanding of the physics behind the low-lying octupole vibrational states in these nuclei [52].
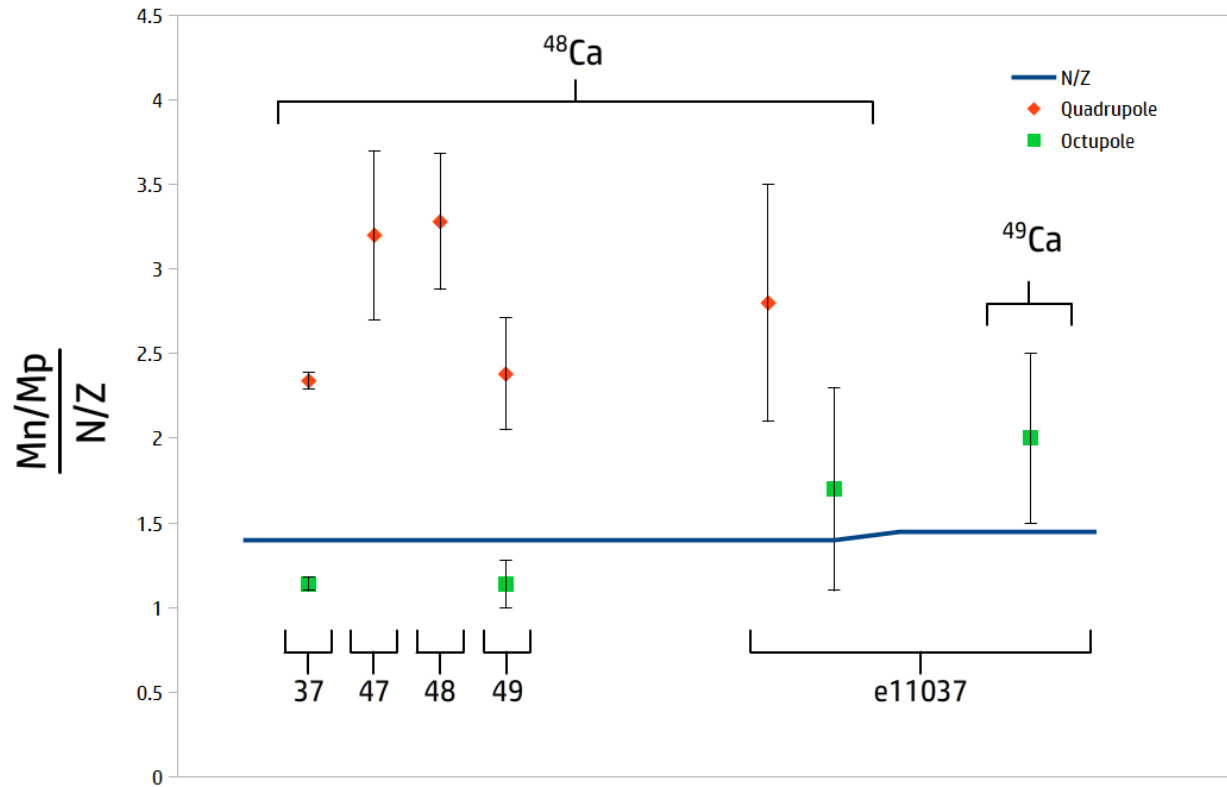
Figure 4.3: Visual representation of the M_n/M_p values from the current experiment and from previous experiments reported in References [1], [2], [3], and [4], with uncertainties shown as error bars. The solid line represents the homogeneous collective model prediction, N/Z, for the ratio M_n/M_p .

Table 4.2: Comparison of M_n/M_p values for the 2_1^+ and 3_1^- states in ^{48}Ca found in literature and derived by the present analysis.

Reaction	Energy [MeV]	2^+ $\frac{M_n}{M_p}$	3^- $\frac{M_n}{M_p}$
$(p,p')^a$	98	2.8(7)	1.7(6)
$(p,p')^b$	200, 318	2.34(5)	1.14(4)
$(p,p')^c$	800	3.2(5)	
$(\alpha,\alpha')^d$	31	3.28(40)	
$(\pi^\pm,\pi^\pm)^e$	180	2.38(33)	1.14(14)

[a]Values generated from data from e11037. 2^+ value generated by Lew Riley [19].

[b]Reference [1].

[c]Reference [2].

[d]Reference [3].

[e]Reference [4].

CHAPTER 5

CONCLUSIONS

As part of the effort to study the suggested $N = 32$ sub-shell closure in neutron rich nuclei near the neutron drip-line, an inverse kinematic proton scattering experiment was performed at the National Superconducting Cyclotron Laboratory using a rare isotope beam containing ^{48,49,50,52}Ca and ^{50}Sc reacting with the Ursinus College liquid hydrogen target. Data was collected during the experiment using the GRETINA-S800 detector system. The primary goal of the experiment was to analyze the low-lying 2^+ states in ^{50,52}Ca, and to compliment this the present analysis discussed in this dissertation focused on analyzing low-lying octupole vibrations in ^{48,49}Ca. In addition, a γ-ray spectroscopic study of reactions of ^{50}Sc with the proton target was also conducted.

The data calibration and sorting software were provided by K. Wimmer and L. Lundberg at the NSCL, and the initial calibration of the data sorting files was performed using the ^{46}Ar isotope present in the secondary isotope beam. The initial analysis started with sorting the data set focused on event timestamps associated with incoming and outgoing ^{49}Ca particles to produce the gated and Doppler-corrected γ-ray spectrum for the inelastic reaction of the proton target with the ^{49}Ca ions. Using GEANT ion simulations to define the appropriate beam energy and thickness of the target, GEANT γ-ray simulations were performed to account for Compton scattering of γ-rays released during the experiment, as well as the configuration of the GRETINA, to produce simulated, Doppler-corrected γ-ray spectraa for each γ-ray decay energy detected during the experiment. The GEANT structure, and associated fitting code templates, were provided by Dr. Lew Riley for use with the analysis. These simulated spectra, along with background approximations, were folded into the fitting code algorithm, channel by channel, to produce a fitted line as close as possible to the measured, Doppler-corrected γ-ray spectrum for ^{49}Ca. The parameters generated by the fitting process represented an accurate number of counts in each γ-ray simulated and detected in coincidence with ^{49}Ca particles.

After encountering issues with the ^{48}Ca data, as well as with the ^{50}Ca data in his own analysis, Riley modified the analysis procedure, specifically in how the GEANT γ-ray spectra were folded into

the fitting process. Using this modified method, the ^{48}Ca reaction data was analyzed. By scaling the GEANT simulated γ-ray spectra to account for the loss of ^{48}Ca particles due to the momentum acceptance of the S800 spectrograph, the fitting process generated parameters ther represented accurate counts in each γ-ray peak detected in coincidence with ^{48}Ca particles. As there had been no discernible issue with the ^{49}Ca data, it was analyzed a second time with the modified analysis method to ensure that the modifications did not introduce unknown systematic errors in the fitting process. The modified analysis method did produce fitted parameters whose value were different from the original method by less than 5%, but that difference was accounted for by the fact that the modified fitting code estimated that about 5% of the ^{49}Ca particles did not make it into the focal plane of the S800. During this phase of the analysis, two new γ-ray peaks were found in the ^{49}Ca data thanks to the diligence of two of the dissertation committee members, the 1431keV and 4469keV γ-rays. After the γ-ray yields for ^{48,49}Ca were finalized, a similar analysis was started for ^{50}Sc. Through a process dubbed "bump-hunting", fifteen new γ-ray peaks were isolated in the Doppler-corrected γ-ray spectrum for ^{50}Sc and fitted to produce γ-ray yields for this isotope. The γ-ray yields for ^{48,49}Ca resulted in the calculation of cross sections for populating the low-lying octupole states in ^{48,49}Ca from the ground state, with values of $\sigma\left(3_1^-,{}^{48}Ca\right) = 6.2(18)$mb, $\sigma\left(\frac{9}{2}_1^+,{}^{49}Ca\right) = 4.2(10)$mb, $\sigma\left(\frac{7}{2}_1^+,{}^{49}Ca\right) = 1.4(3)$mb, and $\sigma\left(\frac{5}{2}_1^+,{}^{49}Ca\right) = 1.4(3)$mb.

The analysis code FRESCO, provided by Dr. Ian Thompson at Lawrence Livermore National Laboratory, was used to produce coupled channels calculations of inelastic reaction cross sections of protons reacting with ^{48,49}Ca. The initial framework was built based on calculations for ^{48}Ca using the analysis code ECIS with the guidance of Dr. Kirby Kemper, and a secondary framework was built for calculations for ^{49}Ca. By matching the measured cross sections from e11037 to the FRESCO calculated inelastic cross sections, the total nuclear deformation length, δ_3 for each of the known octupole vibration lengths in ^{48,49}Ca were extracted from the calculations. These values were found to be $\delta_3\left({}^{48}Ca, 3_1^-\right) = 1.0(2)$fm, $\delta_3\left({}^{49}Ca, \frac{9}{2}_1^+\right) = 1.2(1)$fm, $\delta_3\left({}^{49}Ca, \frac{7}{2}_1^+\right) = 1.5(2)$fm, $\delta_3\left({}^{49}Ca, \frac{5}{2}_1^+\right) = 1.1(1)$fm.

Using lifetime measurements performed by Montanari, $et\ al$, the proton deformation lengths for the lowest-lying octupole vibration excitations for these two nuclei were determined to be $\delta_p\left({}^{48}Ca, 3_1^-\right) = 0.9(1)$fm, $\delta_p\left({}^{49}Ca, \frac{9}{2}_1^+\right) = 1.0(1)$fm [39]. By comparing these proton deformation lengths for these two states to the total nuclear deformation lengths, the neutron deformation

lengths were determined to be $\delta_n \left({}^{48}Ca, 3_1^- \right) = 1.1(3)$fm, and $\delta_n \left({}^{49}Ca, \frac{9}{2}_1^+ \right) = 1.3(3)$fm. In addition to these deformation lengths, the neutron to proton transition matrix element ratio, M_n/M_p , for the lowest-lying octupole vibrations in ^{48,49}Ca were generated: $M_n/M_p \left({}^{48}Ca, 3_1^- \right) = 1.7(6)$ and $M_n/M_p \left({}^{49}Ca, \frac{9}{2}_1^+ \right) = 2.0(5)$.

Unless stated otherwise, all steps of the present analysis described in this dissertation were performed by the author, either independently or under direction by Drs. Lew Riley, Kirby Kemper, Mark Riley, or Paul Cottle. The stability test was specifically developed by the author to determine the reliability of the γ-ray yields. All images in this dissertation were generated by the author and thus have full permission to be reproduced within the context of this dissertation.

The results of the present analysis indicated that the valence neutron in ^{49}Ca coupled to the ^{48}Ca core produces statistically insignificant differences in the lowest-lying octupole vibrations of the proton and neutron components of the ^{49}Ca nucleus. During the course of the analysis, two new γ-rays, 1431keV and 4469keV, were detected and associated with the ^{49}Ca nucleus. Also included in the present analysis was the isolation and identification of fifteen new γ-rays associated with ^{50}Sc.

This dissertation presents analysis of inverse kinematic proton scattering data for ^{48,49}Ca and ^{50}Sc. The analyses for the ^{49}Ca and ^{50}Sc represent the first reported proton scattering experiments for these nuclei, adding to what little nuclear structure data was available for these short-lived isotopes. The present analysis compliments the analysis by Lew Riley geared toward studying the $N = 32$ sub-shell closure in neutron rich nuclei, and will ultimately serve as part of the foundation of data for analysis of shell structure in nuclei toward the neutron drip-line.

Given the relatively large statistical and systematic uncertainties in the present analysis, it would be prudent to revisit this analysis to improve the uncertainties in the neutron deformation lengths and M_n/M_p values. One way to improve the this analysis would be to repeat e11037 while focusing on the production of ^{48,49}Ca rather than ^{50}Ca. This shift in isotope production should substantially improve the production of ^{48,49}Ca as well as the ^{50}Sc. Theoretically, production of ^{49}Sc would also be possible by shifting the production focus to perform an in-depth analysis on the particle-core coupling of a valence proton to the ^{48}Ca core in comparison to the valence neutron for ^{49}Ca. Another prudent departure from e11037 would be to verify that all of the nuclei of interest make it entirely through the S800 momentum acceptance to improve measurements. Beyond this,

it would also be of benefit to perform more extensive reactions with the ^{50}Sc nucleus to enable expansion of the level and decay scheme for this nucleus, which would in turn enable analysis of the low-lying octupole states in this isotope.

The NSCL facilities in the next decade will be replaced after the decommissioning of the K500 and K1200 cyclotrons and the completion of the Facility for Rare Isotope Beams (FRIB). Once in operation, the beam intensities produced by the three Coupled Superconducting Linear Accelerators will be substantially larger in comparisonn to the Coupled Cyclotrons, by an estimated factor of ten at least. This increase in intensity would enable more production of ^{48,49}Ca and ^{49,50}Sc, as well as higher energy ranges. This would enable better statistics for most, if not all, γ-rays detected. Unfortunately, FRIB is currently under construction and will not be capable of producing particle beams until 2022, the expected completion estimate.

BIBLIOGRAPHY

[1] A. E. Feldman, J. J. Kelly, B. S. Flanders, M. A. Khandaker, H. Seifert, P. Boberg, S. D. Hyman, P. H. Karen, B. E. Norum, P. Welch, Q. Chen, A. D. Bacher, G. P. A. Berg, E. J. Stephenson, S. Nanda, A. Saha, and A. Scott. Neutron transition densities for ^{48}Ca from proton scattering at 200 and 318 MeV. *Phys. Rev. C*, 49:2068–2085, Apr 1994.

[2] G. S. Adams, Th. S. Bauer, G. Igo, G. Pauletta, C. A. Whitten, A. Wriekat, G. W. Hoffmann, G. R. Smith, and M. Gazzaly. 800-MeV inelastic proton scattering from ^{40}Ca, ^{48}Ca, and ^{54}Fe. *Phys. Rev. C*, 21:2485–2495, Jun 1980.

[3] A.M. Bernstein, V.R. Brown, and V.A. Madsen. Neutron and proton transition matrix elements and inelastic hadron scattering. *Physics Letters B*, 103(45):255 – 258, 1981.

[4] Kenneth G. Boyer, William B. Cottingame, L. E. Smith, Steven J. Greene, C. Fred Moore, J. S. McCarthy, R. C. Minehart, J. F. Davis, G. R. Burleson, G. Blanpied, Chuck A. Goulding, Henry A. Thiessen, and Christopher L. Morris. Pion inelastic scattering to the low-lying states in ^{42,44,48}Ca: Determination of the neutron and proton multipole matrix elements. *Phys. Rev. C*, 24:598–604, Aug 1981.

[5] R. Tribble, D. Bryman, D. Dean, C. Elster, R. Ent, T. Glasmacher, U. Heinz, X. Ji, R. Lacyey, N. Makins, R. Milner, M. Ramsey-Musolf, H. Nitsche, G. Savard, S. Seestrom, T. Ulrich, U. van Kolck, J. Wilkerson, and W. Zajc. *The Frontiers of Nuclear Science, A Long Range Plan.* Nuclear Science Advisory Committee. United States Department of Energy and National Science Foundation, December 2007.

[6] L. A. Riley and P. D. Cottle. *Inelastic excitations beyond ^{48}Ca.* National Superconducting Cyclotron Laboratory Program Advisory Committy Proposal Form, 2010.

[7] A. Balysh, A. De Silva, V. I. Lebedev, K. Lou, M. K. Moe, M. A. Nelson, A. Piepke, A. Pronskiy, M. A. Vient, and P. Vogel. Double beta decay of ^{48}Ca. *Phys. Rev. Lett.*, 77:5186–5189, Dec 1996.

[8] J. W. Hansen and S. G. Prussin. Precise measurement of the half-life of ^{49}Ca. *The International Journal of Applied Radiation and Isotopes*, 21(6):335 – 338, 1970.

[9] E. K. Warburton, D. E. Alburger, and G. A. P. Engelbertink. Beta decay of K^{47}, Ca^{50}, and Sc^{50}. *Phys. Rev. C*, 2:1427–1433, Oct 1970.

[10] D. E. Alburger, E. K. Warburton, and B. A. Brown. Decays of ^{50}Sc, ^{50}Sc^m, ^{50}Ca, and ^{47}K. *Phys. Rev. C*, 30:1005–1013, Sep 1984.

[11] Lewis A. Riley. *Inverse Kinematics Proton Scattering with a Radioactive ^{18}Ne Beam.* PhD thesis, Florida State University, 1997.

[12] A. M. Bernstein, V. R. Brown, and V. A. Madsen. Neutron and proton matrix elements for low-lying 2^+ transitions and probe dependence of the nuclear deformation parameter. *Comments Nucl. Part. Phys.*, 11:203–215, 1985.

[13] P. Ring and P. Schuck. *The Nuclear Many-Body Problem.* Springer-Verlag, New York, 1980.

[14] D. Goutte, J. B. Bellicard, J. M. Cavedon, B. Frois, M. Huet, P. Leconte, Phan Xuan Ho, S. Platchkov, J. Heisenberg, J. Lichtenstadt, C. N. Papanicolas, and I. Sick. Determination of the transition charge density of the octupole vibration in ^{208}Pb. *Phys. Rev. Lett.*, 45:1618–1621, Nov 1980.

[15] W. T. Wagner, G. M. Crawley, G. R. Hammerstein, and H. McManus. High-resolution study of ^{208}Pb with 35-mev protons. *Phys. Rev. C*, 12:757–777, Sep 1975.

[16] J. W. Hertel, D. G. Fleming, J. P. Schiffer, and H. E. Gove. Coulomb Excitation of the Collective Septuplet at 2.6 MeV in ^{209}Bi. *Phys. Rev. Lett.*, 23:488–491, Sep 1969.

[17] W. T. Wagner, G. M. Crawley, and G. R. Hammerstein. High resolution $(p, p^{'})$ on ^{207}Pb and ^{209}Bi. *Phys. Rev. C*, 11:486–507, Feb 1975.

[18] A1900 Fragment Separator. `https://groups.nscl.msu.edu/a1900/archive/barney/`.

[19] L. A. Riley, M. L. Agiorgousis, T. R. Baugher, D. Bazin, M. Bowry, P. D. Cottle, F. G. DeVone, A. Gade, M. T. Glowacki, K. W. Kemper, E. Lunderberg, D. M. McPherson, S. Noji, F. Recchia, B. V. Sadler, M. Scott, D. Weisshaar, and R. G. T. Zegers. Inverse-kinematics proton scattering on ^{50}Ca: Determining effective charges using complementary probes. *Phys. Rev. C*, 90:011305, Jul 2014.

[20] D. J. Morrissey, B. M. Sherrill, M. Steiner, A. Stolz, and I. Wiedenhoever. Commissioning the A1900 projectile fragment separator. *Nucl. Instrum. Methods B*, 204:90–96, 2003.

[21] L. A. Riley. NSCL Expt 11037. `https://ucnuclear.wikispaces.com/NSCL+Expt+11037`.

[22] S800 Detector Stations. `https://wikihost.nscl.msu.edu/S800Doc/doku.php?id=stations`.

[23] S800 Detectors. `https://wikihost.nscl.msu.edu/S800Doc/doku.php?id=detectors`.

[24] D. Bazin, J.A. Caggiano, B.M. Sherrill, J. Yurkon, and A. Zeller. The {S800} spectrograph. *Nuclear Instruments and Methods in Physics Research Section B: Beam Interactions with Materials and Atoms*, 204(0):629 – 633, 2003. 14th International Conference on Electromagnetic Isotope Separators and Techniques Related to their Applications.

[25] GRETINA Project. http://www.physics.fsu.edu/GRETINA.org/.

[26] GRETINA Proposal. http://www.physics.fsu.edu/GRETINA.org/meetings/Gretina_proposal.pdf, 2003.

[27] J. S. Baron. Utilization of Germanium in Gamma Ray Spectroscopy. Materials Characteristics Project Paper, December 2011.

[28] I.Y. Lee. Gamma-ray tracking detectors. *Nuclear Instruments and Methods in Physics Research Section A: Accelerators, Spectrometers, Detectors and Associated Equipment*, 422(13):195 – 200, 1999.

[29] J. B. A. England. *Techniques in Nuclear Structure Physics*. Halstead Press, New York, 1974.

[30] S. Paschalis, I.Y. Lee, A.O. Macchiavelli, C.M. Campbell, M. Cromaz, S. Gros, J. Pavan, J. Qian, R.M. Clark, H.L. Crawford, D. Doering, P. Fallon, C. Lionberger, T. Loew, M. Petri, T. Stezelberger, S. Zimmermann, D.C. Radford, K. Lagergren, D. Weisshaar, R. Winkler, T. Glasmacher, J.T. Anderson, and C.W. Beausang. The performance of the gamma-ray energy tracking in-beam nuclear array {GRETINA}. *Nuclear Instruments and Methods in Physics Research Section A: Accelerators, Spectrometers, Detectors and Associated Equipment*, 709(0):44 – 55, 2013.

[31] M. Moszyński, J.H. Bjerregard, J.J. Gaardhje, B. Herskind, P. Knudsen, and G. Sletten. Limitation of the Compton suppression in Ge-BGO Compton suppression spectrometers. *Nuclear Instruments and Methods in Physics Research Section A: Accelerators, Spectrometers, Detectors and Associated Equipment*, 280(1):73 – 82, 1989.

[32] K. Vetter, A. Kuhn, I.Y. Lee, R.M. Clark, M. Cromaz, M.A. Deleplanque, R.M. Diamond, P. Fallon, G.J. Lane, A.O. Macchiavelli, M.R. Maier, F.S. Stephens, C.E. Svensson, and H. Yaver. Performance of the GRETA prototype detectors. *Nuclear Instruments and Methods in Physics Research Section A: Accelerators, Spectrometers, Detectors and Associated Equipment*, 452:105 – 114, 2000.

[33] G.J. Schmid, M.A. Deleplanque, I.Y. Lee, F.S. Stephens, K. Vetter, R.M. Clark, R.M. Diamond, P. Fallon, A.O. Macchiavelli, and R.W. MacLeod. A -ray tracking algorithm for the {GRETA} spectrometer. *Nuclear Instruments and Methods in Physics Research Section A: Accelerators, Spectrometers, Detectors and Associated Equipment*, 430(1):69 – 83, 1999.

[34] J. Eberth and J. Simpson. From Ge(Li) detectors to gamma-ray tracking arrays: 50 years of gamma spectroscopy with germanium detectors. *Progress in Particle and Nuclear Physics*, 60(2):283 – 337, 2008.

[35] K. Wimmer and E. Lundberg. NSCL S800 ROOT data analysis. Technical report, National Superconducting Cyclotron Laboratory, Michigan State University, 2013.

[36] S800 map server. `http://maps.nscl.msu.edu/~s800maps/`.

[37] T. W. Burrows. Nuclear Data Sheets for A = 49. *Nucl. Data Sheets*, 109:1879–2032, 2008.

[38] L. A. Riley. Private communication, 2012–2015.

[39] D. Montanari, S. Leoni, D. Mengoni, J. J. Valiente-Dobon, G. Benzoni, N. Blasi, G. Bocchi, P. F. Bortignon, S. Bottoni, A. Bracco, F. Camera, P. Casati, G. Colò, A. Corsi, F. C. L. Crespi, B. Million, R. Nicolini, O. Wieland, D. Bazzacco, E. Farnea, G. Germogli, A. Gottardo, S. M. Lenzi, S. Lunardi, R. Menegazzo, G. Montagnoli, F. Recchia, F. Scarlassara, C. Ur, L. Corradi, G. de Angelis, E. Fioretto, D. R. Napoli, R. Orlandi, E. Sahin, A. M. Stefanini, R. P. Singh, A. Gadea, S. Szilner, M. Kmiecik, A. Maj, W. Meczynski, A. Dewald, Th. Pissulla, and G. Pollarolo. γ spectroscopy of calcium nuclei around doubly magic ^{48}Ca using heavy-ion transfer reactions. *Phys. Rev. C*, 85:044301, Apr 2012.

[40] E. Kashy, A. Sperduto, H. A. Enge, and W. W. Buechner. Shell-model states in Ca^{49}. *Phys. Rev.*, 135:B865–B871, Aug 1964.

[41] R. Broda. High-spin states in and around doubly-magic nuclei. *Acta Phys. Pol. B*, 32:2577–2589, 2001.

[42] R. Broda. Spectroscopic studies with the use of deep-inelastic heavy-ion reactions. *J. Phys. G: Nucl. Part. Phys.*, 32:R151–R192, 2006.

[43] Y. Fujita, M. Fujiwara, S. Morinobu, T. Yamazaki, T. Itahashi, H. Ikegami, and S. I. Hayakawa. Nuclear structure of ^{48}Ca. *Phys. Rev. C*, 37:45–65, Jan 1988.

[44] J. R. Vanhoy, M. T. McEllistrem, Sally F. Hicks, R. A. Gatenby, E. M. Baum, E. L. Johnson, G. Molnár, and S. W. Yates. Neutron and proton dynamics of ^{48}Ca levels and γ-ray decays from neutron inelastic scattering. *Phys. Rev. C*, 45:1628–1643, Apr 1992.

[45] J. E. Wise, J. S. McCarthy, R. Altemus, B. E. Norum, R. R. Whitney, J. Heisenberg, J. Dawson, and O. Schwentker. Inelastic electron scattering from ^{48}Ca. *Phys. Rev. C*, 31:1699–1714, May 1985.

[46] T. R. Canada, C. Ellegaard, and P. D. Barnes. Core excited states in ^{49}Ca studied in the reaction ^{48}Ca$(d, p\gamma)^{49}$Ca*. *Phys. Rev. C*, 4:471–474, Aug 1971.

[47] T. W. Burrows. Nuclear Data Sheets for A = 48. *Nucl. Data Sheets*, 107:1747–1922, 2006.

[48] I. J. Thompson. FRESCO. `http://www.fresco.org.uk/index.htm`.

[49] A. J. Koning and J. P. Delaroche. Local and global nucleon optical models from 1 keV to 200 MeV. *Nucl. Phys. A*, 713:231–310, 2003.

[50] M. A. Kennedy, P. D. Cottle, and K. W. Kemper. Excitations of 2^+_1 and 3^-_1 states from (p,p') and electromagnetic measurements. *Phys. Rev. C*, 46:1811–1817, Nov 1992.

[51] L. A. Riley, M. A. Abdelqader, D. Bazin, M. J. Bojazi, B. A. Brown, C. M. Campbell, J. A. Church, P. D. Cottle, D. C. Dinca, J. Enders, A. Gade, T. Glasmacher, M. Honma, S. Horibe, Z. Hu, K. W. Kemper, W. F. Mueller, H. Olliver, T. Otsuka, B. C. Perry, B. T. Roeder, B. M. Sherrill, T. P. Spencer, and J. R. Terry. Thick-target inverse-kinematics proton scattering from ^{46}Ar and the $n = 28$ shell below ^{48}Ca. *Phys. Rev. C*, 72:024311, Aug 2005.

[52] A. Volya and K. Kravvaris. Private communication, 2012–2015.

BIOGRAPHICAL SKETCH

David Marc McPherson was born Friday, 19 December 1986, in Denton, Texas to Elizabeth Dianne Tate Dunn McPherson and Marc Wickford McPherson, while his older teenage siblings were running around the hospital spreading the mumps. He grew up in the strong household of his mother, attending various primary and secondary schools across Texas. He received his high school diploma from Montwood High School in the top 2% of his graduating class in May 2005.

He started his college career by starting off in a Physics BS degree plan at the University of Texas at El Paso. During the summer of 2009, David participated in the Research Experience for Undergraduates program at the National High Magnetic Field Laboratory at Florida State University. He assisted with two experiments in femtosecond electron diffraction research under the direction of Dr. Jianming Cao. At the end of the program, he presented the research performed at a poster session at the NHMFL. The following fall semester, David participated with the UTEP chapter of the Society for Physics Students in various activities, including the Physics Circus performing physics demonstrations for primary and secondary schools around El Paso. In December 2009, he presented his REU research again in a poster session at the Regional Meeting of the American Physical Society in San Marcos, Texas on behalf of the NHMFL and the UTEP Society of Physics Students. The following March, under the supervision of Dr. Eric Hagedorn, he presented the REU research in the form of a ten minute talk at the Spring Regional Meeting of the American Physical Society in Austin, Texas. David graduated with his Bachelor's of Science Degree in Applied Physics Summa Cum Laude from UTEP in May 2010.

David started his graduate career at Florida State University in August 2010 working toward a PhD in Physics. After completing his base coursework, as well as passing his Written Qualifying Exams, David earned his Master's Degree in Physics from FSU in August 2012. In March 2013, David assisted with an experiment performed at the National Superconducting Cyclotron Laboratory at Michigan State University under the direction of Dr. Ingo Wiedenhover. The following April, David traveled back to the NSCL to assist with the installation, testing, and operation of the Ursinus College liquid hydrogen target for use in three experiments. David was trained to operate the target cell gas handling system during all phases of operation of the target. The experiment used for the analysis presented in this dissertation was the third of these experiments, completed

on May 18th, 2013. In April 2014, David presented his research analysis as it stood at the time in a ten-minute talk to the April Meeting of the American Physical Society in Savannah, Georgia, as well as in front of the entire Nuclear Group in a practice talk during the Nuclear Seminar for the Physics Department. A month later, he also presented his research and research plan, successfully defending his prospectus in front of his advisory committee. In February 2015, David presented his research to the Nuclear Group in a twenty-minute talk during the Nuclear Seminar.

David participated in a few extracurricular activities while at Florida State, including singing in the FSU Men's Glee Club, the Collegians, in over a dozen live performances at locales such as FSU's Oppermann Recital Hall and Ruby Diamond Concert Hall. He also served as a maintenance assistant for the FSU John D. Fox Accelerator Laboratory's 9MV Tandem Accelerator and as a duty shift operator for around two dozen experiments performed at the lab during the course of his doctoral career. He was officially dubbed the "Auxiliary Member of the γ Gang" by the student manager of the γ Cave Group, Jonathan Baron, for assistance in operation of the lab's γ-ray detector system.